Multiplexed neuromodulatory-type-annotated whole-brain EM-reconstruction of larval zebrafish

Fu-Ning Li[1,6], Jia-Zheng Liu[2,6], Can Shi[1,4,6], Jing-Bin Yuan[2,3,6], Ya-Nan Lv[2,3,6], Jing Liu[2,6], Li-Na Zhang[2,6], Lin-Lin Li[2,6], Li-Jun Shen[2,6], Xi Chen[2,6], Hao Zhai[2,3], Bo-Hao Chen[2,3], Yan-Chao Zhang[2,3], Jin-Yue Guo[2,3], Hao-Ran Chen[2,3], Hai-Yang Yan[2,3], Sheng Chang[2], Hong-Tu Ma[2], Fang-Xu Zhou[2], Tong Xin[2], Xiao-Hui Dong[2], Li-Mei Lin[2], Xing-Hui Zhao[2], Qi-Wei Xie[2], Zheng-Huan Fang[1], Jia-Liang Zu[1,4], Rong-Kun Tao[1], Han-Yang Hu[1], Chen-Ying Qian[1], Yan-Song Wang[1,4], Chang-Mei Zhang[1], Pei-Shan Xiang[1], Yong-Xin Yang[1], Yu Qian[1], Yu-chen Gong[1], Xu-Fei Du[1], Hua Han[2,3,*] & Jiu-Lin Du[1,4,5,7,*]

[1] Institute of Neuroscience, State Key Laboratory of Brain Cognition and Brain-Inspired Intelligence Technology, Center for Excellence in Brain Science and Intelligence Technology, Chinese Academy of Sciences, 320 Yue-Yang Road, Shanghai 200031, China

[2] State Key Laboratory of Brain Cognition and Brain-Inspired Intelligence Technology, Institute of Automation, Chinese Academy of Sciences, Beijing 100190, China

[3] School of Future Technology, School of Artificial Intelligence, University of Chinese Academy of Sciences, Beijing 101408, China

[4] University of Chinese Academy of Sciences, 19A Yu-Quan Road, Beijing 100049, China

[5] School of Life Science and Technology, ShanghaiTech University, 319 Yue-Yang Road, Shanghai 200031, China

[6] These authors contributed equally to this work

[7] Lead contact

* Correspondence

Dr. Jiu-Lin Du,
Institute of Neuroscience,
Chinese Academy of Sciences,
Shanghai 200031, China
E-mail: forestdu@ion.ac.cn

Dr. Hua Han,
Institute of Automation,
Chinese Academy of Sciences,
Beijing 100190, China
E-mail: hua.han@ia.ac.cn

The brain is complementarily assembled by the sensorimotor and neuromodulatory (NM) pathways[1]. While connectome mapping is crucial for elucidating the synaptic organization principles underlying this bi-pathway architecture, most electron microscopy (EM) reconstructions provide limited information about cell types, particularly NM neurons[2-7]. Here we present Fish-X, a synapse-level, multiplexed NM-type-annotated reconstruction of an intact larval zebrafish brain, identifying noradrenergic, dopaminergic, serotonergic, hypocretinergic, and glycinergic neurons via subcellular localization of peroxidase APEX2, with glutamatergic/GABAergic neurons inferred through morphology comparison with the Zebrafish Mesoscopic Atlas. NM neurons with varying indegree scale-distinctly innervate various sensory – motor brain regions that exhibit heterogeneity in synapse number and strength. Whereas some NM neurons receive localized unitary inputs, individual locus coeruleus noradrenergic (LC-NE) neurons integrate brain-wide inputs with modality-specific spatial organization: Motor inputs converge proximally, while sensory inputs favor distal dendrites of these neurons. LC-NE neurons receive distinct yet overlapping inputs—while most presynaptic neurons establish exclusive one-to-one connections, a specialized subset broadcasts divergent projections to multiple LC-NE targets, creating a hierarchical control architecture. Notably, these shared input patterns extend across monoaminergic systems, suggesting a structural basis for coordinated neuromodulation. Based on the first vertebrate brain-wide EM reconstruction with multiplexed NM-type annotation, our study demonstrate the synaptic organization principles of the LC-NE system's inputome. Integrated with multi-modal mesoscopic data[8], Fish-X offers a valuable resource with various precisely identified NM types, and a critical reference for elucidating synaptic organization principles of bi-pathway architecture in vertebrate brains.

Introduction

Brain function is underpinned by exquisitely organized architectural principles that operate across various scales, ranging from the precise spatial localization of synapses to the intricate morphologies of individual neurons and the characteristic connectivity patterns among distinct brain regions. The synaptic-resolution connectome represents a foundational challenge in neuroscience, offering a mechanistic framework to bridge structure, function, and behavior[9-12]. While complete wiring diagrams have been achieved for small invertebrate nervous systems[5,7], vertebrate whole-brain connectomics remains incomplete—despite landmark achievements in mouse and human cortical reconstructions[3,4,13-19]. Zebrafish (*Danio rerio*) larvae now emerge as the most tractable vertebrate model for whole-brain connectomics, combining manageable brain scale with conserved circuit architecture. Pioneering work has mapped local circuits[20-23] or generated whole-brain datasets[2,6,24], yet existing datasets often possess limited resolution or omit essential input-output regions—notably the retina (sensory entry) and spinal cord (motor output)—limiting systems-level interrogation of sensorimotor transformation.

The functional complexity of neural networks arises not only from their physical wiring, but also from the molecular diversity of their constituent neurons. Molecular defined neuronal types serve as crucial bridges linking static structural data with dynamic functional readouts. Recent light-microscopy-based connectomics

(LICONN) highlights the field's urgent need for molecular annotated connectomes[25]. Traditional volume electron microscopy (vEM)-based connectomics has primarily relied on prior structural features for neuronal classification, including stereotyped somata positioning, projection morphologies, specialized cellular structures, and synaptic ultrastructures. For neuronal populations with less well-characterized structural signatures, cell-type identification has been achieved mainly through correlative light-electron microscopy (CLEM), genetically encoded tags for EM (GETEM) and immuno-EM. Beyond a few well-studied excitatory and inhibitory populations (e.g., cortical pyramidal neurons in mouse; reticulospinal neurons in zebrafish), the majority of cell types—particularly neuromodulatory (NM) populations—lack sufficient ground-truth data for structural feature extraction. For these challenging cases, GETEM currently represents the most handy annotation approach, enabling precise molecular identification within synaptic-resolution wiring diagrams without complex computations[26].

To address this, we presented Fish-X, a brain-wide, synapse-level, multiplexed molecular annotated vEM dataset spanning from the retina to the anterior spinal cord in 6-day post-fertilization (dpf) larval zebrafish. The dataset features noradrenergic, dopaminergic, serotonergic, hypocretinergic (also known as orexinergic), and glycinergic neurons that were genetically labeled using enhanced ascorbate peroxidase 2 (APEX2) targeted to distinct subcellular compartments, driven by cell-type-specific promoters[27-32]. Additionally, several excitatory (E) glutamatergic and inhibitory (I) GABAergic neurons were inferred through the Zebrafish Mesoscopic Atlas[8]-assisted morphology comparison. Leveraging the unique advantages of the multiplexed molecular annotated ssEM dataset, we systematically investigated perisomatic and synaptic characteristics across neuronal types, with focus on monoaminergic systems. Heterogeneous features — including nuclear-to-cytoplasmic volume ratio, perisomatic mitochondrial density, dendritic indegree—extracted from genetically-labeled ground truth enable identification of unlabeled neurons both in this study and in other zebrafish connectome datasets.

NM neurons with varying indegree exhibited scale-distinct innervation patterns across various sensory－motor brain regions that displayed heterogeneity in synapse number and strength. Whereas some NM neurons exhibited localized innervation for local neuromodulation, others possessed widespread projections enabling multi-regional neuromodulation. Through brain-wide synapse-level reconstruction, we tackled a fundamental question regarding the bi-pathway brain architecture: where NM neurons receive upstream inputs and how these inputs are spatially organized at synaptic resolution. As a pivotal hub for whole-brain activity modulation[33-43], a single LC-NE neuron integrated brain-wide inputs with modality-specific spatial organization. Besides, we revealed the modular organization of dendritic inputs in the LC-NE system, where most presynaptic neurons innervated single LC-NE neurons while a minority form divergent connections with multiple LC-NE neurons. Notably, diverse monoaminergic systems also shared common inputs, suggesting a modular inputome architecture that supports coordinated neuromodulation among noradrenergic, dopaminergic, and serotonergic systems.

Fish-X offers a valuable synapse-level, whole-brain resource featuring a variety of precisely annotated molecular types. Together with other intriguing zebrafish connectomics studies, which include E/I annotations and calcium functional profiles obtained through CLEM, Fish-X has contributed to the foundational infrastructure that encompasses sample preparation, algorithms, proofreading platforms, and public sharing.

This infrastructure is essential for future whole connectome reconstruction. Furthermore, Fish-X demonstrates synergistic potential with multi-modal mesoscopic datasets, such as the Zebrafish Mesoscopic Atlas. It not only enhances the annotation of neuronal types in EM connectomes but also facilitates the analysis of synaptic connectivity among specific neurons, with their morphology traced in functional studies. Collectively, Fish-X serves as a critical reference for deciphering the principles of synaptic organization within the bi-pathway architecture of vertebrate brains.

Results

Whole-brain ssEM of APEX2-labeled larval zebrafish

We utilized peroxidase APEX2[31], which catalyzes hydrogen peroxide (H_2O_2)-dependent polymerization and localized deposition of diaminobenzidine (DAB), to enable EM labeling of molecularly defined neuronal types. APEX2 was targeted to distinct subcellular compartments via signal peptides driven by cell-type-specific promoters, to achieve multiplexed labeling in individual brains. We generated a fish line, *Gt(vmat2:GAL4FF);Tg(dbh:GAL4FF;UAS:cytosol-APEX2-TagRFP);Tg(hcrt:APEX2-TagRFP-NLS);Tg(glyt2:MITO-APEX2-TagRFP)*, in which APEX2 was specifically targeted to (i) the cytoplasm in monoaminergic neurons (noradrenergic, NE; dopaminergic, DA; serotonergic, 5HT), (ii) the nucleus in hypocretinergic (Hcrt) neurons, and (iii) the mitochondria in glycinergic (Gly) neurons (Fig. 1a; Extended Data Fig. 1; see Methods for details). To evaluate labeling efficiency, we crossed the APEX2 fish lines with multiple published stable lines and compared fluorescence expression patterns. The APEX2 fish lines successfully labeled target nuclei in the locus coeruleus (LC), medulla oblongata (MO), olfactory bulb (OB), posterior tuberculum (PT), caudal hypothalamus (Hc), pretectum (Pr), superior/inferior raphe (SR/IR), Hypothalamus (Hyp), and hindbrain as expected, though with varying labeling efficiency. This variability may result from differential APEX2 expression levels caused by random insertion of genetic sequences in the Tol2-based transgenic system (Extended Data Fig. 1d).

Using the automated tape-collecting ultramicrotome – scanning electron microscopy (ATUM-SEM) approach[24,44], we acquired a whole-brain serial-section electron microscopy (ssEM) dataset at $4 \times 4 \times 33$ nm^3 per voxel resolution along the rostrocaudal axis, extending from the olfactory epithelium to the anterior spinal cord (third myomere) in a 6-dpf multiplexed APEX2-labeled larva (Extended Data Fig. 2a; see Methods for details). The imaged volume, generated from 22,901 consecutive coronal-view ultrathin sections, encompassed ~3.1160×10^7 μm^3 for the central brain, ~5.5620×10^4 μm^3 for the right optic nerve, and ~6.0877×10^6 μm^3 for the right retina (Fig. 1b).

We identified 176,810 cells in the brain through convolutional neural network (CNN)-based three-dimensional (3D) automated nucleus segmentation (see Methods for details), with subsequent manual proofreading. In comparison, manual cell counting in the right retina yielded 70,910 cells. Additionally, we automatically identified 25.25 million postsynaptic densities (PSDs), 15.77 million synaptic vesicle clouds (SVs), and 13.73 million mitochondria, respectively (see Methods for details). At the macroscopic level, the brain exhibits a bilaterally symmetrical architecture. Neuronal tracts with varying sizes served as highways for inter-regional signal transmission, among which only the reticulospinal system, lateral line system, and optic nerve (partially) displayed significant myelination (Fig. 1c). Besides, the vascular network responsible for

nutrient supply and metabolic waste clearance was predominantly localized within the neuropil region (77.78% of the reconstructed volume localized within neuropil) (Fig. 1c). Somata were predominantly localized in the medial-dorsal soma regions (94.59% of the total cell population), while the lateral-ventral neuropil, containing sparse cells, provided spaces for synaptic crosstalk (Fig. 1d,e). Using a CNN-based approach, we generated automated 3D reconstructions of the brain (Extended Data Fig. 2b,c; see Methods for details). Manual proofreading was then performed using our custom Advanced Connectome Engine (ACE) platform, which enabled large-scale data management and supported collaborative online proofreading by multiple proofreaders (see Methods for details). Our study focused on the reconstruction of multiple APEX2-labeled NM neurons and their presynaptic partners, particularly within monoaminergic systems (Fig. 1f).

Neuron classification via multi-strategy approaches

For neuronal classification, we first employed a CLEM approach to align the ssEM dataset with the region-annotated template brain from the Zebrafish Mesoscopic Atlas[8], followed by identification via multi-strategy approaches (Fig. 2a; Extended Data Fig. 2a; see Methods for details). All cells in the brain and retina were mapped to their corresponding regions. Significant variations in soma density were observed across brain regions (Extended Data Fig. 3a,b; Supplementary Table 1,2). For instance, in the brain, the neuropil layers (NL) and periventricular cell layer (PL) in optic tectum exhibited the minimum and maximum soma densities (0.51 vs. 10.62 per 10^3 μm^3), respectively. In contrast, in the retina, outer nuclear layer (ONL), the inner nuclear layer (INL), and retinal ganglion cell layer (RGCL) all demonstrated higher soma densities (12.18, 21.01, 15.63 per 10^3 μm^3, respectively; Extended Data Fig. 3a). This structural differences suggest a more compact cytoarchitecture in the retina, which also partially explains why most zebrafish EM studies fail to acquire both brain and retina data simultaneously—the substantial density differences pose significant technical challenges for reagent infiltration and continuous ultrathin sectioning.

We integrated distinct EM-visible perisomatic signatures with soma location to classify and quantify APEX2-labeled neurons (Fig. 2a,b; Extended Data Fig. 1a). Since most monoaminergic nuclei are discretely localized, we classified individual neurons as NE, DA, or 5HT based on their soma location, despite the shared *vmat2*-driven cytoplasmic APEX2 labeling. Hcrt and Gly neurons were classified based on nuclear- and mitochondrial-localized APEX2, respectively. In total, we identified at least five molecular types across 9 nuclei/regions ($n_{LC\text{-}NE}$ = 12, $n_{MO\text{-}NE}$ = 54, $n_{OB\text{-}DA}$ = 47, $n_{PT\text{-}DA}$ = 22, $n_{Hc\text{-}DA}$ = 45, $n_{Pr\text{-}5HT}$ = 9, $n_{SR/IR\text{-}5HT}$ = 117, n_{Hcrt} = 12, and n_{Gly} neurons = 4,019). Specifically, due to the abundant population of Gly neurons, we trained a neural network to automatically segment APEX2-labeled mitochondria and subsequently identified Gly neurons based on the number of APEX2-labeled mitochondria within their somata (see Methods for details). All other APEX2-labeled nuclei were manually quantified by expert proofreaders. Integrating deep-learned and traditional features, the whole-brain nucleus analysis revealed generally continuous distributions in clustering space, though vasculature-associated cell types (e.g. endothelial cells, EC; pericytes, PC; red blood cells, RBC) aggregated. This segregation became more pronounced when nucleus clustering was performed using only 1,169 cells that had been manually annotated for cell types (Extended Data Fig. 3c,d). We systematically investigated the nuclear features of various APEX2-labeled neuronal types and

manually-annotated vasculature-associated cell types, finding that their nuclei exhibited diverse 3D morphologies. Neuronal nuclei typically exhibited spherical or ellipsoidal morphologies, compared with the flattened, sheet-like nuclei of vasculature-associated cells and the irregular shapes observed in some undefined cell types. Among APEX2-labeled neurons, long-projecting neuronal types (e.g., LC-NE/PT-DA) displayed larger nuclei. Additionally, some neuronal types possessed nuclei with obvious shallow grooves (e.g., LC-NE) or deep infoldings (e.g., Gly) (Extended Data Fig. 3e).

Next, we tested whether structural features extracted from APEX2-labeled neurons could serve as ground truth to classify corresponding types of neurons lacking APEX2 labeling. Given that most cells remain incomplete fragments after automated reconstruction, neuronal classification based on local structural features allows for the rapid and precise targeting of specific neuronal populations, followed by targeted proofreading[45]. For instance, LC-NE neurons exhibited not only larger nuclear volumes but also larger somata, extensive endoplasmic reticulum (ER), a quantity of mitochondria, and specialized cilia (Fig. 2c). Quantitative analysis revealed that LC-NE neurons had a lower nuclear-to-somatic volume ratio (0.4123 ± 0.0808 vs. 0.6530 ± 0.0113) and a higher somatic mitochondrial density (0.5449 ± 0.0496 vs. 0.0843 ± 0.0088 per 1 μm^3) than adjacent randomly selected cells. These distinct perisomatic features enabled precise discrimination between NE and non-NE cells withing the LC region (Fig. 2d). Subsequent clustering analysis integrating both nuclear and somatic characteristics further validated this observation (Fig. 2e). Based on these criteria, we identified an additional unlabeled LC-NE neuron in the right hemisphere, whose morphological features closely match those of the APEX2-labeled LC-NE neurons (Fig. 2f). We extended this analysis to other APEX2-labeled neuronal types and found that PT-DA neurons could similarly be identified based solely on localized perisomatic features. The remaining neuronal types exhibited no significant ultrastructural differences from neighboring cells, indicating the need to incorporate additional features, such as complete morphology and synaptic characteristics, for precise identification without genetic labeling (Extended Data Fig. 3f,g). Notably, LC-NE neurons displayed the highest somatic mitochondrial density among all APEX2-labeled neuronal populations, suggesting an adaptive coordination between their subcellular energetic infrastructure and brain-wide projection patterns/functional demands.

In principle, we could achieve simultaneous labeling of additional molecularly-defined neuronal types (e.g., glutamatergic and GABAergic) by generating a super fish line with more APEX2-transgenes through further crossings. However, as previously noted, given that synaptic and neuronal morphologies represent another fundamental intrinsic characteristics, we investigated whether synapse clustering or morphology comparison—using mesoscopically fully traced neurons of known types—could facilitate the classification of additional neuronal populations in the Fish-X dataset. For synaptic clustering, we examined an additional EM dataset featuring mitochondrial labeling in glutamatergic and GABAergic neurons. Our quantitative analysis revealed that glutamatergic and GABAergic synapses showed no significant differences in PSD thickness or volume, with only minor exceptions in rare individual cases (Extended Data Fig. 4). Considering the high requirements for both image quality and alignment accuracy in PSD morphological analysis, we instead pursued neuronal-type inference via morphology comparison. We utilized the Zebrafish Mesoscopic Atlas as the reference, which contains ~20,000 fully reconstructed mesoscopic morphologies of both excitatory (E) and inhibitory (I) neurons ($n_{vglut2a/2b}$ = 12,219, n_{gad1b} = 5,371, n_{glyt2} = 2,193) (Fig. 2a). For each EM-reconstructed

query neuron, which was pre-registered to the mesoscopic template brain through a CLEM pipeline, we extracted mesoscopic data within a 25-μm radius sphere centered at its geometric centroid. Subsequent skeleton matching against these references yielded penalty scores and allowed type inference based on morphological similarity (see Methods for details). The lower the penalty score, the higher the similarity. The entire pipeline has now been incorporated into our custom all-in-one platform, Brain Atlas Viewer (BrAVe). We sorted the top-10 candidates and manually verified through BrAVe. We utilized 491 presynaptic neurons of the LC-NE system as a test case. Notably, this approach proved effective, despite the fact that most of these neurons were not fully reconstructed (Fig. 2g,h). For some EM query neurons, the top-10 candidates were exclusively either glutamatergic or GABAergic neurons, enabling high-confidence E/I identity inference. In comparison, other query neurons showed E/I mixed candidates among their top-10 matches, suggesting either limited discriminability between E/I neurons within these brain regions, or the need for more complete reconstructions of these EM neurons (Fig. 2i). Furthermore, we observed APEX2-labeled mitochondria in some query neurons that were independently inferred as glycinergic neurons by micro-mesoscopic skeleton matching, demonstrating both the feasibility and reliability of this cross-modal comparison approach (Fig. 2j).

Region- and neuron type-specific synaptic heterogeneity

Various neuronal types are synaptically interconnected, collectively forming an integrated entity that executes diverse neurophysiological functions. To investigate the connectivity properties of diverse neuronal types, we first systematically investigated the densities of all synapse-related components across brain regions. The results revealed highly consistent brain-region-level distribution patterns across PSDs, SVs and mitochondria (Extended Data Fig. 5; Supplementary Table 3,4,5). The significant quantitative disparities among the three components suggest distinct fine-scale spatial distribution patterns. We therefore further identified the presynaptic and postsynaptic automatically segmented supervoxels of individual PSDs, while also assigning SVs and mitochondria to their respective spatially associated supervoxels. We demonstrated that ~56.6% of PSDs were spatially associated with both SVs and mitochondria, whereas ~36.9% of PSDs co-existed with SVs but lacked mitochondria (Fig. 3a). To minimize interference from misidentified instances in automated segmentation results during analysis, we defined typical synapses by the co-occurrence of PSDs at postsynaptic sites and SVs at presynaptic sites. Surprisingly, we found ~39.5% of typical synapses lacked mitochondria. Given mitochondria's critical roles in energizing synaptic functions, their presence may serve as a potential marker of functional synapses in static EM datasets. Besides, mitochondria exhibited a higher isolation ratio (Fig. 3a). Combined with their observed presence in both non-synaptic processes and somata, these findings suggest highly functional heterogeneity within mitochondrial populations. Further quantification of the densities of typical synapses across brain regions revealed a negative correlation (R^2 = 0.7070, $P < 0.0001$) between synapse distribution and soma distribution, reinforcing principles of spatial segregation within the brain (Fig. 3b,c). Specifically, synapses were predominantly localized in neuropil regions, while soma regions contained sparse synapses. Interestingly, when we incorporated features associated with synapse strength (including the volumes of PSDs, SVs, and mitochondria) into our analysis, we found that all three synapse strength-related characteristics followed lognormal distributions across all brain regions (Fig. 3d-g). Notably, we observed regional variations in distribution profiles. For instance, some

regions, such as lobus caudalis cerebelli (LCa) and epiphysis (E), exhibited sharply peaked PSD volume distributions, whereas others, such as habenula (Ha), showed broader distributions, suggesting potential variations in synaptic organization principles. More balanced distributions of synapse strengths may contribute to either more complex neural computations or enhanced plasticity, while rarer strong synapses may enable higher signal-to-noise ratios.

As noted previously, neuropil regions serve as the primary sites for synaptic communication, necessitating matched neuromodulation by specific NM systems. Mesoscopic projectome analysis revealed distinct region-specific innervation patterns among different NM neuronal types (Extended Data Fig. 6). For instance, LC-NE neurons displayed widespread broadcasting projections throughout the brain, while OB-DA neurons demonstrated spatially restricted innervation. We manually reconstructed somatodendritic morphologies for multiple NM neurons in the right hemisphere and validated their presynaptic input sites (Fig. 3h,i). In total, we verified 8,042 synaptic inputs for 44 APEX2-labeled neurons. Dendrites were manually identified based on synaptic input locations for the subsequent calculation of dendritic input densities. Although heterogeneity in dendritic input density existed within each neuronal type, the three monoaminergic nuclei—LC-NE, PT-DA, and SR-5HT—collectively exhibited higher average synaptic input density (Fig. 3k). In contrast, while the Mauthner cell similarly displayed high indegree, they were distinct in receiving substantial synaptic inputs on its soma (Fig. 3j).

Input organization principles of the LC-NE system

A fundamental question regarding NM pathways is where NM neurons receive their presynaptic inputs and how these inputs are spatially organized. We used the LC-NE system as a model to address this scientific question. As a key node in regulating brain-wide neural networks, the convergent input organization of LC-NE populations has been revealed by viral-genetic tracing[46,47]. However, how brain-wide inputs conveying distinct physiological information are spatially organized on their dendrites remains poorly understood. We traced all presynaptic neurons originating from the dendritic input sites of a single LC-NE neuron (LC-NE #3), which exhibited the longest dendrites (~1.812 mm) and the highest dendritic indegree ($n_{synapse}$ = 560). We successfully traced 75% of these synaptic inputs ($n_{synapse}$ = 418) back to their somata (Fig. 4a). Notably, a single LC-NE neuron received widespread presynaptic inputs from 27 brain regions, with a dominant preference for motor-related regions in hindbrain, particularly in rhombomere 1 (R1, Fig. 4b). In contrast, some NM neurons, such as OB-DA and Pr-5HT neurons, received inputs that were spatially constrained within unitary neuropil regions, suggesting relatively modality-specific neuromodulation (Extended Data Fig. 7). Integrated analysis of synaptic spatial positions and their corresponding soma locations revealed that LC-NE neurons implemented modality-dependent spatial organization of dendritic inputs. Motor-related and sensory-related inputs preferentially target proximal and distal dendrites of these neurons, respectively (motor-related, 103.3 ± 2.480 μm; sensory-related, 122.8 ± 3.210 μm; Fig. 4c,d,e). Although these dendritic inputs showed no significant differences in either PSD volume or SV volume (Fig. 4d,e), in vivo calcium imaging of somatodendritic activity demonstrated significantly stronger responses to motor-related events compared to pure auditory or visual stimuli (Fig. 4f,g,h). This phenomenon was reminiscent of observations in mouse cortical pyramidal neurons, where apical dendritic inputs exert regulatory control over the effects of

feedforward inputs targeting proximal dendrites, enabling context-dependent dendritic integration[48].

Recent studies support the heterogeneous and modular organization of the LC-NE system[49-51]. Our results that individual LC-NE neurons shared distinct yet overlapping dendritic inputs, further reinforcing the concept of LC-NE system heterogeneity. For instance, we identified that LC-NE neuron #4 specifically received Hcrt inputs (Extended Data Fig. 8), while most glycinergic neurons targeted only single LC-NE neurons. Besides, a minority of presynaptic neurons, named common presynaptic inputs (CPI), innervated at least two LC-NE neurons (Fig. i-k). These neurons may function as an important neural substrate underlying the synchronous activity observed in LC-NE neuronal populations[33,52,53], potentially serving to coordinate their functional outputs under specific behavioral or physiological conditions. Interestingly, CPIs exhibited varying divergence degrees, with most innervating 2 LC-NE neurons (Fig. 4l,m). Moreover, we also identified CPIs across monoaminergic systems (Fig. 4n-p). Specific inter-CPIs simultaneously innervate any two of LC-NE, PT-DA, and SR-5HT neurons (Fig. 4q,r). We conducted in vivo calcium imaging on these monoaminergic nuclei simultaneously and discovered that some of LC-NE and PT-DA neurons indeed exhibited synchronous spontaneous activities. In contrast, the synchrony associated with SR-5HT neurons was not as pronounced, as these nuclei were relatively silent (Fig. 4s,t). Analysis of E/I identities revealed that 75% (6/8) of inter-CPIs between LC-NE and PT-DA neurons were inferred as glutamatergic, whereas 50% (9/18) of inter-CPIs between LC-NE and SR-5HT neurons were GABAergic. We hypothesized that LC-NE and PT-DA neurons might receive shared feedforward driving signals, whereas LC-NE and SR-5HT neurons could be subject to common inhibitory modulatory inputs. These inter-CPIs may constitute the structural basis for coordinated activity across distinct monoaminergic modules, enabling more diversified neuromodulation. In summary, leveraging this multiplexed NM-type-annotated, synapse-level whole-brain EM dataset, we mapped brain-wide inputs to individual LC-NE neurons, revealing modality-dependent spatially organization. Furthermore, we demonstrated LC-NE populations received distinct yet overlapping synaptic inputs within the LC-NE system and shared common innervation across monoaminergic systems, to generate modular neuromodulatory effects with varying intensities and neuromodulator combinations (Fig. 4u).

Discussion

In this study, we present a brain-wide, synapse-level, multiplexed molecular annotated vEM dataset of larval zebrafish. The dataset extends beyond the brain to include the unilateral retina, optic nerve, and partial spinal cord, providing a unique resource for investigating sensorimotor transformations, particularly for visual processing pathways.This is particularly valuable considering the zebrafish as a visually dominant species, where the number of cells in a single retina is more than one-third that of the entire brain. While CNN-based automated reconstruction has been completed for the brain, extensive manual proofreading remains essential for achieving a truly validated whole-brain connectome. With ongoing improvements in online collaborative proofreading systems, we can now systematically map input – output architectures of key neuromodulatory systems. Furthermore, rapidly advancing AI-for-Science (AI4S) technologies will enable dataset realignment and resegmentation, significantly enhancing connectome validation efficiency. Importantly, our ATUM-SEM approach has preserved all sectioned samples intact, allowing for future acquisition of currently unmapped extracerebral structures to expand this resource.

Our dataset features multiplexed molecular annotation. Using a subcellular compartment-targeted APEX2 strategy, we have achieved the simultaneous labeling of at least five molecularly defined neuronal types, including four important neuromodulatory neuronal populations across eight corresponding nuclei. For non-APEX2-labeled neuronal classes, such as glutamatergic and GABAergic neurons, we have established a feasible framework for inferring E/I identities through mesoscopic atlas-assisted skeleton comparison, combined with synaptic ultrastructural features. While perisomatic and synaptic ultrastructural features have been demonstrated to enable precise cell-type identification[45,54], vertebrate connectomics has been hampered by the lack of sufficient ground-truth references, particularly for neuromodulatory neurons. Our dataset provides readily identifiable and reliable EM-visible markers, from which structural signatures of corresponding neuronal classes have been extracted. These signatures can not only facilitate the complementary identification of unlabeled individuals within our dataset but also enable broader application to other zebrafish vEM datasets.

This study represents the first successful implementation of multiplexed APEX2 labeling in an intact vertebrate brain. An alternative approach to molecular annotation utilizes CLEM, a method whereby distinct neuronal populations are fluorescently labeled and subsequently correlated with EM data. This approach directly leverages existing zebrafish transgenic lines and typically produces high-quality images, as hydrogen peroxide is not required for sample preparation. In comparison, the GETEM strategy exemplified by APEX2 offers distinct advantages: (i) identifiability without complex registration calculations, (ii) multiplexed molecular annotation through orthogonal multi-compartment labeling that overcomes the spectral constraints of fluorescent proteins, and (iii) suitability for distal/long-range axonal labeling in local EM reconstructions where complete neuronal morphologies are unavailable. Although the APEX2-DAB reaction introduces technical challenges throughout sectioning, imaging, and reconstruction, it indeed drives substantial improvements in real-time quality control with targeted re-imaging, image repairing, image denoising, and semi-automated reconstruction of labeled neurons. These optimizations will significantly enhance future sample processing efficiency and data fidelity. More importantly, the above two strategies can be used in combination—the fluorescent signals from APEX2-fused proteins exhibit perfect correspondence with their EM-visible counterparts generated through APEX2 catalysis, serving as matching landmarks that simplify CLEM registration. Furthermore, we demonstrate the feasibility of a molecular annotation strategy based on cross-modal dataset alignment. Compared to vEM, the light-microscopy-based mesoscopic atlas features neuronal type-specific promoter-driven sparse fluorescent labeling, enabling more efficient and cost-effective acquisition of vast datasets containing complete morphological profiles of known neuronal types. By matching the reconstructed skeletons or morphological features (whether partial or complete) from vEM data with these mesoscopic references, we can reliably infer molecular identities. Collectively, these complementary strategies will significantly advance our understanding of structural characteristics across diverse neuronal types, ultimately contributing to the comprehensive reconstruction of a molecular annotated whole-brain connectome in zebrafish.

This study elucidates the significance of molecular annotated connectomics in deciphering brain architecture through the lens of the LC-NE system. As an evolutionarily conserved hub regulating brain-wide states and behavioral performance, the LC-NE system receives convergent inputs and broadcasts information

widely, while accumulating evidence reveals its modular functional organization. Through relatively comprehensive reconstruction of presynaptic inputs onto single LC-NE neurons, we demonstrate that individual LC-NE neurons integrate brain-wide inputs exhibiting modality- and strength-specific spatial organization: motor-related inputs with stronger synapse strength preferentially target proximal dendrites, while non-motor-related weaker inputs predominantly innervate distal dendrites. Whether this proximal – distal dichotomy corresponds to phasic – tonic firing patterns requires further investigation[55]. Similar to cortical pyramidal neurons where apical dendritic inputs modulate proximal inputs, we postulate comparable interactive mechanisms in LC-NE neurons — their activity strongly correlates with motor output, while non-motor-related inputs adjust the gain of motor-related signals, enabling brain-state-dependent modulation. Thus, the LC-NE system not only broadcasts noradrenergic signals globally but also monitors whole-brain activity through extensive inputs to self-tune its regulatory efficacy. The predominantly one-to-one connectivity, along with one-to-many connectivity typically targeting 2 – 3 LC-NE neurons, further supports functional modularity, whereas rare common inputs innervating most LC-NE neurons, combined with previously reported electrical synapses, may synchronize population activity for specific functions requiring massive norepinephrine release. Shared input patterns across monoaminergic systems reveal combinatorial neuromodulator co-release mechanisms, highlighting complex inter-system interactions and underscoring the value of multiplexed molecular annotated connectomics. Future work will focus on monoaminergic systems to delineate their inputome and outputome organizations underlying coordinated neuromodulation beyond the canonical bi-pathway architecture.

References

1. Li FN, Zhang CM, Du JL. Neuromodulatory processing in the bi-pathway brain architecture. *Curr Opin Neurobiol*. Published online May 23, 2025. doi:10.1016/j.conb.2025.103055
2. Petkova M, Januszewski M, Blakely T, et al. A connectomic resource for neural cataloguing and circuit dissection of the larval zebrafish brain. *bioRxiv*. doi:10.1101/2025.06.10.658982
3. MICrONS Consortium. Functional connectomics spanning multiple areas of mouse visual cortex. *Nature*. 2025;640(8058):435-447. doi:10.1038/s41586-025-08790-w
4. Shapson-Coe A, Januszewski M, Berger DR, et al. A petavoxel fragment of human cerebral cortex reconstructed at nanoscale resolution. *Science*. 2024;384(6696):eadk4858. doi:10.1126/science.adk4858
5. Dorkenwald S, Matsliah A, Sterling AR, et al. Neuronal wiring diagram of an adult brain. *Nature*. 2024;634(8032):124-138. doi:10.1038/s41586-024-07558-y
6. Svara F, Förster D, Kubo F, et al. Automated synapse-level reconstruction of neural circuits in the larval zebrafish brain. *Nat Methods*. 2022;19(11):1357-1366. doi:10.1038/s41592-022-01621-0
7. Cook SJ, Jarrell TA, Brittin CA, et al. Whole-animal connectomes of both Caenorhabditis elegans sexes. *Nature*. 2019;571(7763):63-71. doi:10.1038/s41586-019-1352-7
8. Du XF, Yue ZF, Wei JF, et al. Central nervous system atlas of larval zebrafish constructed using the morphology of single excitatory and inhibitory neurons. *bioRxiv*. doi:10.1101/2025.06.06.658008
9. Boulanger-Weill J, Kämpf F, Schuhknecht GFP, et al. Correlative light and electron microscopy reveals the fine circuit structure underlying evidence accumulation in larval zebrafish. *bioRxiv*.

425 doi:10.1101/2025.03.14.643363
426 10. Brittin CA, Cook SJ, Hall DH, et al. A multi-scale brain map derived from whole-brain volumetric
427 reconstructions. *Nature*. 2021;591(7848):105-110. doi:10.1038/s41586-021-03284-x
428 11. Ngai J. BRAIN 2.0: Transforming neuroscience. *Cell*. 2022;185(1):4-8. doi:10.1016/j.cell.2021.11.037
429 12. Lichtman JW, Pfister H, Shavit N. The big data challenges of connectomics. *Nat Neurosci*.
430 2014;17(11):1448-1454. doi:10.1038/nn.3837
431 13. Celii B, Papadopoulos S, Ding Z, et al. NEURD offers automated proofreading and feature extraction for
432 connectomics. *Nature*. 2025;640(8058):487-496. doi:10.1038/s41586-025-08660-5
433 14. Gamlin CR, Schneider-Mizell CM, Mallory M, et al. Connectomics of predicted Sst transcriptomic types
434 in mouse visual cortex. *Nature*. 2025;640(8058):497-505. doi:10.1038/s41586-025-08805-6
435 15. Wang EY, Fahey PG, Ding Z, et al. Foundation model of neural activity predicts response to new
436 stimulus types. *Nature*. 2025;640(8058):470-477. doi:10.1038/s41586-025-08829-y
437 16. Ding Z, Fahey PG, Papadopoulos S, et al. Functional connectomics reveals general wiring rule in mouse
438 visual cortex. *Nature*. 2025;640(8058):459-469. doi:10.1038/s41586-025-08840-3
439 17. Dorkenwald S, Schneider-Mizell CM, Brittain D, et al. CAVE: Connectome Annotation Versioning
440 Engine. *Nat Methods*. 2025;22(5):1112-1120. doi:10.1038/s41592-024-02426-z
441 18. Schneider-Mizell CM, Bodor AL, Brittain D, et al. Inhibitory specificity from a connectomic census of
442 mouse visual cortex. *Nature*. 2025;640(8058):448-458. doi:10.1038/s41586-024-07780-8
443 19. Gour A, Boergens KM, Heike N, et al. Postnatal connectomic development of inhibition in mouse barrel
444 cortex. *Science*. 2021;371(6528):eabb4534. doi:10.1126/science.abb4534
445 20. Vishwanathan A, Sood A, Wu J, et al. Predicting modular functions and neural coding of behavior from a
446 synaptic wiring diagram. *Nat Neurosci*. 2024;27(12):2443-2454. doi:10.1038/s41593-024-01784-3
447 21. Friedrich RW, Wanner AA. Dense Circuit reconstruction to understand neuronal computation: focus on
448 zebrafish. *Annu Rev Neurosci*. 2021;44:275-293. doi:10.1146/annurev-neuro-110220-013050
449 22. Vishwanathan A, Daie K, Ramirez AD, et al. Electron Microscopic Reconstruction of Functionally
450 Identified Cells in a Neural Integrator. *Curr Biol*. 2017;27(14):2137-2147.e3.
451 doi:10.1016/j.cub.2017.06.028
452 23. Wanner AA, Genoud C, Masudi T, et al. Dense EM-based reconstruction of the interglomerular
453 projectome in the zebrafish olfactory bulb. *Nat Neurosci*. 2016;19(6):816-825. doi:10.1038/nn.4290
454 24. Hildebrand DGC, Cicconet M, Torres RM, et al. Whole-brain serial-section electron microscopy in larval
455 zebrafish. *Nature*. 2017;545(7654):345-349. doi:10.1038/nature22356
456 25. Tavakoli MR, Lyudchik J, Januszewski M, et al. Light-microscopy-based connectomic reconstruction of
457 mammalian brain tissue. *Nature*. 2025;642(8067):398-410. doi:10.1038/s41586-025-08985-1
458 26. Shigemoto R, Joesch M. The genetic encoded toolbox for electron microscopy and connectomics. *Wiley*
459 *Interdiscip Rev Dev Biol*. 2017;6(6):10.1002/wdev.288. doi:10.1002/wdev.288
460 27. Zhang Q, Lee WA, Paul DL, et al. Multiplexed peroxidase-based electron microscopy labeling enables
461 simultaneous visualization of multiple cell types. *Nat Neurosci*. 2019;22(5):828-839.
462 doi:10.1038/s41593-019-0358-7
463 28. Cruz-Lopez D, Ramos D, Castilloveitia G, et al. Quintuple labeling in the electron microscope with

464 genetically encoded enhanced horseradish peroxidase. *PLoS One*. 2018;13(7):e0200693. Published 2018
465 Jul 16. doi:10.1371/journal.pone.0200693
466 29. Joesch M, Mankus D, Yamagata M, et al. Reconstruction of genetically identified neurons imaged by
467 serial-section electron microscopy. *Elife*. 2016;5:e15015. Published 2016 Jul 7. doi:10.7554/eLife.15015
468 30. Böhm UL, Prendergast A, Djenoune L, et al. CSF-contacting neurons regulate locomotion by relaying
469 mechanical stimuli to spinal circuits. *Nat Commun*. 2016;7:10866. Published 2016 Mar 7.
470 doi:10.1038/ncomms10866
471 31. Lam SS, Martell JD, Kamer KJ, et al. Directed evolution of APEX2 for electron microscopy and
472 proximity labeling. *Nat Methods*. 2015;12(1):51-54. doi:10.1038/nmeth.3179
473 32. Atasoy D, Betley JN, Li WP, et al. A genetically specified connectomics approach applied to long-range
474 feeding regulatory circuits. *Nat Neurosci*. 2014;17(12):1830-1839. doi:10.1038/nn.3854
475 33. Zhang CM, Yang YX, Li FN, et al. Multiple-level organizational logic of the locus
476 coeruleus-norepinephrine system in structure and function. *bioRxiv*. doi:10.1101/2025.06.11.659024
477 34. Poe GR, Foote S, Eschenko O, et al. Locus coeruleus: a new look at the blue spot. *Nat Rev Neurosci*.
478 2020;21(11):644-659. doi:10.1038/s41583-020-0360-9
479 35. Zerbi V, Floriou-Servou A, Markicevic M, et al. Rapid Reconfiguration of the Functional Connectome
480 after Chemogenetic Locus Coeruleus Activation. *Neuron*. 2019;103(4):702-718.e5.
481 doi:10.1016/j.neuron.2019.05.034
482 36. Chandler DJ, Jensen P, McCall JG, et al. Redefining Noradrenergic Neuromodulation of Behavior:
483 Impacts of a Modular Locus Coeruleus Architecture. *J Neurosci*. 2019;39(42):8239-8249.
484 doi:10.1523/JNEUROSCI.1164-19.2019
485 37. Foote SL, Berridge CW. New developments and future directions in understanding locus coeruleus -
486 Norepinephrine (LC-NE) function. *Brain Res*. 2019;1709:81-84. doi:10.1016/j.brainres.2018.09.033
487 38. Totah NK, Neves RM, Panzeri S, et al. The Locus Coeruleus Is a Complex and Differentiated
488 Neuromodulatory System. *Neuron*. 2018;99(5):1055-1068.e6. doi:10.1016/j.neuron.2018.07.037
489 39. Sara SJ. The locus coeruleus and noradrenergic modulation of cognition. *Nat Rev Neurosci*.
490 2009;10(3):211-223. doi:10.1038/nrn2573
491 40. Bouret S, Sara SJ. Network reset: a simplified overarching theory of locus coeruleus noradrenaline
492 function. *Trends Neurosci*. 2005;28(11):574-582. doi:10.1016/j.tins.2005.09.002
493 41. Aston-Jones G, Cohen JD. An integrative theory of locus coeruleus-norepinephrine function: adaptive
494 gain and optimal performance. *Annu Rev Neurosci*. 2005;28:403-450.
495 doi:10.1146/annurev.neuro.28.061604.135709
496 42. Berridge CW, Waterhouse BD. The locus coeruleus-noradrenergic system: modulation of behavioral state
497 and state-dependent cognitive processes. *Brain Res Brain Res Rev*. 2003;42(1):33-84.
498 doi:10.1016/s0165-0173(03)00143-7
499 43. Usher M, Cohen JD, Servan-Schreiber D, et al. The role of locus coeruleus in the regulation of cognitive
500 performance. *Science*. 1999;283(5401):549-554. doi:10.1126/science.283.5401.549
501 44. Hayworth KJ, Morgan JL, Schalek R, et al. Imaging ATUM ultrathin section libraries with WaferMapper:
502 a multi-scale approach to EM reconstruction of neural circuits. *Front Neural Circuits*. 2014;8:68.

503 Published 2014 Jun 27. doi:10.3389/fncir.2014.00068
504 45. Elabbady L, Seshamani S, Mu S, et al. Perisomatic ultrastructure efficiently classifies cells in mouse
505 cortex. *Nature*. 2025;640(8058):478-486. doi:10.1038/s41586-024-07765-7
506 46. Schwarz LA, Miyamichi K, Gao XJ, et al. Viral-genetic tracing of the input-output organization of a
507 central noradrenaline circuit. *Nature*. 2015;524(7563):88-92. doi:10.1038/nature14600
508 47. Schwarz LA, Luo L. Organization of the locus coeruleus-norepinephrine system. *Curr Biol*.
509 2015;25(21):R1051-R1056. doi:10.1016/j.cub.2015.09.039
510 48. Suzuki M, Larkum ME. General Anesthesia Decouples Cortical Pyramidal Neurons. *Cell*.
511 2020;180(4):666-676.e13. doi:10.1016/j.cell.2020.01.024
512 49. Uematsu A, Tan BZ, Ycu EA, et al. Modular organization of the brainstem noradrenaline system
513 coordinates opposing learning states. *Nat Neurosci*. 2017;20(11):1602-1611. doi:10.1038/nn.4642
514 50. Hirschberg S, Li Y, Randall A, et al. Functional dichotomy in spinal- vs prefrontal-projecting locus
515 coeruleus modules splits descending noradrenergic analgesia from ascending aversion and anxiety in rats.
516 *Elife*. 2017;6:e29808. Published 2017 Oct 13. doi:10.7554/eLife.29808
517 51. Chandler DJ, Gao WJ, Waterhouse BD. Heterogeneous organization of the locus coeruleus projections to
518 prefrontal and motor cortices. *Proc Natl Acad Sci U S A*. 2014;111(18):6816-6821.
519 doi:10.1073/pnas.1320827111
520 52. Ishimatsu M, Williams JT. Synchronous activity in locus coeruleus results from dendritic interactions in
521 pericoerulear regions. *J Neurosci*. 1996;16(16):5196-5204. doi:10.1523/JNEUROSCI.16-16-05196.1996
522 53. Christie MJ, Williams JT, North RA. Electrical coupling synchronizes subthreshold activity in locus
523 coeruleus neurons in vitro from neonatal rats. *J Neurosci*. 1989;9(10):3584-3589.
524 doi:10.1523/JNEUROSCI.09-10-03584.1989
525 54. Eckstein N, Bates AS, Champion A, et al. Neurotransmitter classification from electron microscopy
526 images at synaptic sites in Drosophila melanogaster. *Cell*. 2024;187(10):2574-2594.e23.
527 doi:10.1016/j.cell.2024.03.016
528 55. Grimm C, Duss SN, Privitera M, et al. Tonic and burst-like locus coeruleus stimulation distinctly shift
529 network activity across the cortical hierarchy. *Nat Neurosci*. 2024;27(11):2167-2177.
530 doi:10.1038/s41593-024-01755-8
531

532 **Methods**

533 **Zebrafish husbandry**

534 Adult Zebrafish (*Danio rerio)* were kept in a circulating system at 28℃ under a 14:10 hour light-dark cycle.
535 All animal protocols were reviewed and approved by the Animal Care and Use Committee of the Center for
536 Excellence in Brain Science and Intelligence Technology, Chinese Academy of Sciences (NA-046-2023).
537 Larvae were fed with *Brachionid* rotifers from 4.5 – 9 dpf, then switched to freshly hatched *Artemia* nauplii
538 thereafter. The sex of embryonic and larval zebrafish was undetermined.
539

540 **Zebrafish lines**

541 All transgenic zebrafish larvae are in *nacre* background. The *vmat2*, *dbh*, *th1*, *tph2*, *hcrt*, *vglut2a*, *gad1b*, *glyt2*

promoters were used to label monoaminergic, noradrenergic, noradrenergic/dopaminergic, serotonergic, hypocretinergic, glutamatergic, GABAergic, and glycinergic neurons, respectively. Published fish lines used in this study include: *Tg(UAS:mCherry)zf408* (*abbreviation*: *Tg(UAS:mCherry)*)[56], *Tg(slc6a5:GFP)cf3* (*Tg(glyt2:GFP)*)[57], *Tg(-2.0Fru.Hcrt:EGFP)zf11* (*Tg(Hcrt:EGFP)*)[58], *Tg(5×UAS:EGFP)nkuasgfp1a* (*Tg(5×UAS-TATA:EGFP)*)[59], *Tg(elavl3:Hsa.H2B-GCaMP6f)jf7* (*Tg(HuC:H2B-GCaMP6f)*)[60], *Tg(5×UAS-hsp70l:GCaMP6s)nkUAShspzGCaMP6s13a* (*Tg(UAS:GCaMP6s)*)[61], *Ki1(th:EGFP)ion27d* (*Ki1(th:EGFP)*)[62], *Ki(th:GAL4-VP16)ion32d* (*Ki(th:GAL4-VP16)*)[62], *Ki(tph2:EGFP)ion39d* (*Ki(tph2:EGFP)*)[62], *Ki(dbh:GAL4-VP16)ion36d* (*Ki(dbh:GAL4-VP16)*)[63], *Tg(slc17a6:GAL4FF)ion177d* (*Tg(vglut2a:GAL4FF)*)[63]. Unpublished fish lines include: *TgBAC(gad1b:GAL4-VP16)* was provided by Dr. Jie He and *gSAIzGFFM242A* (*Gt(vmat2:GAL4FF)*) was provided by Dr. Koichi Kawakami. *Ki(tph2:GAL4FF,myl7:EGFP)ion127d* (*Ki(tph2:GAL4FF,cmlc2:EGFP)*) was constructed using CRISPR/Cas9-based knockin[62], while *Tg(slc6a5:Hsa.Cox8a-APEX2-TagRFP)ion97d* (*Tg(glyt2:MITO-APEX2-TagRFP)*), *Tg(hcrt:APEX2-TagRFP-NLS)ion100d* (*Tg(hcrt:APEX2-TagRFP-NLS)*), and *Tg(dbh:GAL4FF;5×UAS-hsp:cytosol-APEX2-TagRFP)ion142d* (*Tg(dbh:GAL4FF;UAS:cytosol-APEX2-TagRFP)*) were constructed using Tol2 system[64]. The *APEX2* sequence was cloned from the commercial plasmid *Bact2-APEX2-GBP* (Addgene, Cat# 67668)[65]. *glyt2*, *hcrt*, and *dbh* promoter sequences were cloned from plasmids *pTol2-glyt2-P2A-ECFP*, *pTol2-hcrt-GAL4-VP16*, *pTol2-dbh (short)-GAL4FF-5XUAS-hsp-TRPV1-RFPT*, respectively. Additionally, we generated the plasmid *5×UAS-2×Cox8a-APEX2-TagRFP* to specifically label mitochondria in glutamatergic and GABAergic neurons via the GAL4-UAS system. Signal peptide sequences are listed below.

Nuclear localization sequence (*3×NLS*):

TACCTTTCTCTTCTTTTTTGGATCTACCTTTCTCTTCTTTTTTGGATCTACCTTTCTCTTCTTTTTTGG

Cytochrome c oxidase subunit 8A (*MITO*; labeled as *2×Cox8a* in plasmid):

ATGTCCGTCCTGACGCCGCTGCTGCTGCGGGGCTTGACAGGCTCGGCCCGGCGGCTCCCAGTGCC
GCGCGCCAAGATCCATTCGTTGGGGGATCTGTCCGTCCTGACGCCGCTGCTGCTGCGGGGCTTGA
CAGGCTCGGCCCGGCGGCTCCCAGTGCCGCGCGCCAAGATCCATTCGTTG

Immunostaining

Larvae were fixed overnight on a shaker at 4℃ using 4% paraformaldehyde (PFA, Sigma, Cat# 158127) prepared in phosphate-buffered saline (PBS). Following three 5-min washes with PBS containing 1% Tween-20 (PBST), brains was carefully dissected using fine forceps and subjected to another three PBST washes. Samples then underwent graded dehydration/rehydration through sequential incubation in (v/v): 25% methanol/75% PBST (5 min, RT), 50% methanol/50% PBST (5 min, RT), 75% methanol/25% PBST (5 min, RT), 100% methanol (4 h, -20℃), followed by reverse gradient to 25% methanol, then three 5-min PBST washes at RT. After ddH_2O rinse (5 min, RT) and acetone treatment (10 min, -20℃), samples were rehydrated through ddH_2O and three final PBST washes. Blocking was performed overnight at 4℃ (or 4 h at RT) with gentle shaking, followed by incubation with primary antibodies (1:200 in blocking buffer) at 4℃ for 24 – 48 h. After primary antibody recovery and three quick PBST rinses, extended washing was performed (2 × 1 h, 1 × 20 min, 1 × 10 min). Secondary antibodies (1:500 in blocking buffer) were applied at 4°C for 36 h, followed

581 by removal, three quick PBST washes, and final rinses (3 × 10 min, 1 × 30 min) before light-protected storage
582 on ice for fluorescence imaging. Commercial antibodies included: Anti-Orexin-A antibody (Millipore, Cat#
583 AB3704), Anti-Tyrosine Hydroxylase antibody (Millipore, Cat# MAB318), and Goat anti-rabbit IgG H&L
584 Alexa Fluor® 488 (Abcam, Cat# AB150077).
585
586 **In vivo structural and functional imaging**
587 At 3 dpf, multiplexed APEX2-labeled larvae were initially screened using an upright fluorescence
588 stereomicroscope, followed by embedding in 1.5% low-melting-point agarose (Invitrogen, Cat# 15517014) at
589 5 dpf for precise verification of APEX2 fluorescent signals under an upright fluorescence microscope to
590 localize cytoplasmic labeling in monoaminergic neurons, nuclear labeling in hypocretinergic neurons, and
591 mitochondrial labeling in glycinergic neurons, while simultaneously evaluating individual labeling efficiency
592 to select ideal specimens for further EM sample preparation. At 6 dpf, larvae were paralyzed with 1 mg/mL
593 α-bungarotoxin (Tocris, Cat# 2133) and dorsally embedded in 1.5% low-melting-point agarose.
594 Morphological fluorescence imaging was performed using an upright laser scanning confocal microscope
595 (FV3000, Olympus, Japan) equipped with a 40× water-immersion objective (NA = 0.8). Imaging parameters
596 included a frame size of 635.9 × 635.9 μm² (0.621 × 0.621 μm^2 per pixel), with two-field stitching along the
597 rostrocaudal axis to cover the spinal cord, Z-axis intervals of 1 – 1.5 μm, and 2 – 3 line averaging. Selected
598 brain regions were further imaged at higher zoom factors to achieve enhanced spatial resolution when
599 required.
600 We conducted functional calcium imaging on the somata and subjacent dendrites of population LC-NE
601 neurons in 6-dpf *Ki(dbh:GAL4-VP16);Tg(UAS:GCaMP6s);Tg(UAS:mCherry)* larvae, using an upright
602 two-photon fluorescence microscope (FVMPE-RS, Olympus, Japan) equipped with a 25× water-immersion
603 objective (NA = 1.05). Imaging parameters included a frame size of 127.3 × 74.8 μm² (0.250 × 0.250 μm^2 per
604 pixel), with resonant scanning mode, excitation wavelength at 920 nm, imaging depth of ~100 μm, Z-axis
605 intervals of 10 μm, volumetric imaging rate at ~5 Hz, and total acquisition duration of ~3 min per session.
606 During imaging, visual stimuli (red flash, 500 ms) and auditory stimuli (90 dB, 100 ms) were manually
607 delivered, with precise timing recorded via a Digidata 1440A (Molecular Devices, USA). Electromyography
608 (EMG) was simultaneously recorded to identify motor-related calcium events in the paralyzed specimen.
609 Somatic calcium responses were measured from the peak post-stimulus activity in a single cell, whereas
610 dendritic responses were calculated as the average peak post-stimulus activity across ~100 dendritic arbors
611 from a population LC-NE neurons. To simultaneously record calcium dynamics in multiple neuronal
612 populations including LC-NE, SR-5HT, and PT-DA neurons, we performed functional calcium imaging on
613 6-dpf *Ki(th:GAL4-VP16);Ki(tph2:GAL4FF,cmlc2:EGFP);Tg(UAS:GCaMP6s)* larvae, using confocal
614 microscope FV3000. Imaging parameters included a frame size of 636.4 × 636.4 μm² (1.243 × 1.243 μm^2 per
615 pixel), with resonant scanning mode, imaging depth of ~200 μm, Z-axis intervals of 10 μm, volumetric
616 imaging rate at ~0.72 Hz, and total acquisition duration of ~30 min per session.
617
618 **DAB staining**
619 The optimized DAB staining protocol was adapted from published procedures[66]. The 0.1 M Tris-HCl buffer

(pH 7.4) was prepared by dissolving 0.6055 g Tris-Base (Millipore, Cat# 648311) in 50 mL of ultrapure water, with pH adjustment using concentrated HCl. A 10 mg tablet of 3,3'-diaminobenzidine tetrahydrochloride (DAB·4HCl, Sigma, Cat# D5905) was subsequently dissolved in 10 mL of this buffer through vigorous vortexing under light-protected conditions. The solution was then filtered through a 0.22-μm membrane (Millipore, Millex^{TM}-GP 0.22-μm filter) to obtain a 1 mg/mL DAB stock solution, which was stored at 4℃ and protected from light. Samples were sequentially rinsed on a 4℃ shaker or on ice with: (1) 0.1 M phosphate buffer (3 × 10 min), (2) Tris-HCl buffer (2 × 10 min), and (3) DAB solution (2 × 10 min) to remove residual aldehydes. For the reaction, 1 μL of 30% H_2O_2 (Sinopharm Chemical Reagent Co., Ltd., Cat# 10011218) was mixed with 1 mL DAB stock to prepare the working solution, after which samples were incubated for 2 h at RT in complete darkness. The reaction was terminated by washing with Tris-HCl buffer (2 × 10 min). The catalysis by APEX2 of DAB polymerization resulted in dark brown precipitates, which were clearly visible under bright-field stereomicroscopy. Post-fixation with osmium tetroxide was conducted immediately following DAB staining to preserve the osmiophilic reaction products.

EM sample preparation

A mixed fixative containing 2% PFA and 2% glutaraldehyde (GA) was used for effective whole-brain fixation. A 1 mL aliquot of 25% GA (Sigma, Cat# G5882, stored at -20℃) was thawed at 4℃ under light protection. Concurrently, 1 g PFA powder was dissolved in 20 mL of ultrapure water within a fume hood, with 1 – 2 drops of 1 M NaOH added. The solution was then sealed, protected from light, and heated at 65℃ with magnetic stirring until fully clarified. After cooling to RT, the solution was filtered through a 0.22 μm membrane to yield 5% PFA stock. The 10-mL working fixative was prepared immediately before dissection by mixing 4 mL of 5% PFA, 0.8 mL of 25% GA, 5 mL of 0.1 M phosphate buffer (pH 7.4), and 0.2 mL of ultrapure water. Larvae were embedded in 1.5% low-melting-point agarose (Invitrogen, Cat# 15517014) dissolved in extracellular solution (in mM: 134 NaCl, 2.9 KCl, 2.1 $CaCl_2·2H_2O$, 1.2 $MgCl_2·6H_2O$, 10 HEPES, 10 glucose; 290 mOsm, pH 7.8). The agarose covering dorsal epidermis and pectoral fins was removed. Using glass micropipettes, the skin was carefully dissected from the hindbrain ventricle while avoiding damage to vascular/neural tissues. The trunk was rapidly transected anterior to the swim bladder using ophthalmic scissors, after which the head was gently extracted with fine forceps and immediately immersed in fresh fixative. Fixed samples were sealed and stored at 4℃ in darkness overnight.

Subsequent procedures followed the rOTO protocol[67,68]. First, a 1:1 (v/v) mixture of 0.2 M phosphate buffer and 2% OsO_4 (TED PELLA, Cat# 18451) was prepared to obtain an OsO_4-phosphate solution, which was then used to prepare a reduced OsO_4-phosphate solution containing 0.03 g/mL potassium hexacyanoferrate trihydrate (Sigma, Cat# P9387). All OsO_4-containing solutions were freshly prepared within a fume hood, tightly sealed, protected from light at 4℃, and properly collected for disposal after use. Fixed samples were washed with 0.1 M phosphate buffer at 4℃ (4 × 10 min) and then immersed in the OsO_4-phosphate solution (200 – 500 μL per 1.5 mL tube, 2 h, 4℃). Concurrently, a 0.01 g/mL aqueous thiocarbohydrazide (TCH, Sigma, Cat# 88535) solution was placed in a 60℃ oven and gently flipped to facilitate dissolution. The TCH solution was removed from the oven and allowed to cool slightly above RT before use. The solution was then filtered through a 0.22 μm membrane directly into the sample tube that had

been rinsed with ultrapure water (3 × 10 min, 4℃; 1 × 10 min, RT). After a 30-min light-protected TCH treatment at RT, samples were washed with ultrapure water (4 × 10 min, 4℃). The reduced OsO_4-phosphate solution was then added (200 – 500 μL per 1.5 mL tube, 30 min, RT). Afterward, samples were washed with ultrapure water (4 × 10 min, 4℃). Meanwhile, a 2% aqueous uranyl acetate solution (EMS, Cat# 22400) was centrifuged at 13,000 rpm, and the supernatant was carefully transferred into the sample tube (200 μL per 1.5 mL tube). Samples were then sealed and stored at 4℃ overnight, protected from light.

The next day, the uranyl acetate waste solution was collected for proper disposal, followed by washing samples with ultrapure water (3 × 10 min). Subsequently, a graded dehydration series was performed on ice using ethanol solutions (30%, 50%, 70%, 80%, 90%, 95%, and 100% v/v, each for 10 min) followed by anhydrous acetone (2 × 10 min). On the day of fixation, the resin volume was calculated, and the premix was prepared by sequentially pipetting 10 mL of Pon-812 epoxy resin monomer (SPI, Cat# 90529-77-4), 3.36 mL of dodecenyl succinic anhydride (DDSA, SPI, Cat# 26544-38-7), and 7.04 mL of nadic methyl anhydride (NMA, SPI, Cat# 25134-21-8) into a pre-dried tube at RT to form a three-component premix. This was then sealed and mixed on a rotary mixer for at least 3 hours. Resin infiltration was conducted immediately following dehydration. 400 μL DMP-30 epoxy accelerator (SPI, Cat# 90-72-2) was added to 20 mL premix, followed by 30-min rotary mixing to prepare the final resin solution. The resin solution was either used immediately after a 30-min bubble-settling period or kept mixing to prevent polymerization at RT. Samples underwent graded acetone-resin infiltration at ratios of 3:1, 1:1, and 1:3 (v/v) for 8 h, 8h, and overnight, respectively. They were then transferred to vials filled with resin and subjected to vacuum-assisted horizontal shaking using a 5 mL syringe. This process was conducted over two days with resin changes occurring twice daily at intervals of 8 – 12 h. All procedures were performed under controlled environmental conditions (temperatures < 25℃; humidity < 30%). Following the two-day resin infiltration, samples were transferred to pre-dried 21-well flat molds and oriented using sterile toothpicks. The molds were then placed in a drying box containing silica gel beads and polymerized at 37℃ for 8 – 12 h. After verifying and minimally adjusting sample orientation at night, the temperature was increased to 45℃ overnight, then to 60℃ the next morning. Fully polymerized blocks were removed from the oven after 48 h and stored in a dry cabinet.

X-ray tomography

X-ray microscopy (XRM) imaging was utilized with the Xradia 520 Versa system (Zeiss, Germany) at the Instrumental Analysis Center of Shanghai Jiao Tong University to rapidly and non-destructively evaluate the quality of whole-brain EM samples from larval zebrafish. Samples exhibiting uniform staining, minimal deformation, and no apparent mechanical damage were selected for subsequent ultrathin sectioning and SEM imaging. Following resin trimming, samples were scanned at 60 kV with 1 μm^3 voxel resolution (~2 h per sample). Data processing was conducted using Dragonfly (Object Research Systems, Canada). Sequential images were imported with resampling parameters and voxel resolution specified. Sample orientation was interactively manipulating reference axes in the display window. Selected views were exported as projection sequences via the "*Derive new from current view*" function. 3D animations were created using the *Video marker* tool.

698 **Whole-brain ultrathin section collection**

699 Using an ultramicrotome equipped with an automated tape-collecting system (ATUMtome, RMC, USA),
700 serial sections were obtained with thicknesses ranging from 30 to 35 nm[24,44]. Prior to collection, trimmed
701 excess blank resin around the larva using a double-edged razor blade. The front guide slot of the ATUMtome
702 was properly positioned, and parameters including sectioning speed (0.8 mm/s), tape-advancing speed (0.6
703 mm/s), and water refilling interval (5-second durations every 8 minutes) were set. The anti-static device and
704 intermittent water replenishment system were activated to ensure sequential and stable section collection on
705 hydrophilic, conductive polyimide film strips (KAPTON-PET, DuPont, USA). If section instability is
706 observed during collection (e.g., incomplete sections), immediately halt sectioning and either reposition the
707 knife edge or replace the diamond knife (UltraMaxi, Diatome, Switzerland). Throughout the process, ambient
708 conditions were maintained at ~25℃ and 60% humidity. Following collection, section-bearing strips were
709 segmented and mounted onto 4-inch monocrystalline silicon wafers using 0.8-mm-wide conductive adhesive
710 tape (SPI, USA), with careful pressing to eliminate air bubbles. The mounted wafer was placed into a LEICA
711 EM ACE 600 high-vacuum coater for carbon deposition (6 – 10 nm film thickness). The section surfaces were
712 cleaned using nitrogen gas blowing, and subsequently stored in a dry cabinet at 25℃ and 30% humidity.

713 The whole-brain ultrathin section library of larval zebrafish comprised 22,901 serial sections along the
714 rostrocaudal axis, with an average thickness of 33 nm. The entire collection process, which required three
715 days and utilized three diamond knives, yielded an overall damage rate of 6.56% (1,503 sections with folds,
716 tears, and severe contamination, which were algorithmically repaired to ensure intact portions were accurately
717 registered to adjacent sections[69]). Notably, caudal sections obtained later in the collection process exhibited a
718 proportionally higher damage rate, accounting for 77.0% of all compromised sections (1,158/1,503). The
719 retinal region also displayed a higher damage rate, primarily due to the significant structural differences
720 between the eye and brain tissues. The majority of defects did not occur at identical locations across adjacent
721 sections, thus collectively posing no substantial impact on proofreading. Note that sections 6319, 9819, and
722 16958 exhibited losses of 2 – 3 sections, for which experts performed validation of reconstructions across
723 these regions.

724

725 **SEM image acquisition**

726 To enhance sample stability and backscattered electron (BSE) signal contrast, wafers were uniformly
727 pre-irradiated using a custom-built irradiation system (9 mA, 2 kV, 10 s continuous exposure). Post-irradiation
728 wafers were transferred to an optical microscope (Clippers FBT, China) for the acquisition of navigation
729 images via line-scan rapid imaging with 7.6 μm pixel resolution. High-throughput image acquisition was
730 conducted simultaneously across three SEMs (Navigator NeuroSEM100, FBT, China), each equipped with a
731 custom-built collection software designed to maximize efficiency in image output. The pixel resolution was
732 set to 4 nm, the dwell time to 43.5 ns, and the acceleration voltage to 2 kV. Auto focus and astigmatic
733 correction were configured to 80 s per section. To expedite acquisition efficiency and imaging success rate, a
734 systematic region-specific focusing protocol coupled with photography was implemented. Each section was
735 divided into a grid of ~54 tiles (arranged in 9 rows × 6 columns) at 12,000 × 12,000 pixels per tile. To ensure
736 accurate stitching, the adjacent tiles were acquired with a 12% overlapping region. 16 tiles (4 × 4 arrangement)

constituted one standard region. Edge regions containing fewer than 16 tiles were processed equivalently. Regions were sequentially numbered (e.g., region 1) and navigated in a serpentine pattern. Prior to high-resolution scanning, a low-resolution focus was conducted to ensure the algorithm's efficacy in pinpointing the optimal focal range at the center of the section, which was set at a resolution of 50 nm with a dwell time of 80 ns. The stage then precisely oriented to the first region's center for high-resolution focusing and astigmatism correction with a resolution of 4 nm and a dwell time of 80 ns, followed by snake-pattern tile acquisition. After capturing all tiles within a region, the stage advanced to the next region (2.5 s/tile for positional adjustment and data transfer). This cycle iterated until full-section coverage was achieved, maintaining serpentine navigation between regions. The process repeated automatically for subsequent sections until wafer-wide imaging completion.

To enhance the accuracy and robustness of large-scale EM image processing, we introduced an image quality assessment and tissue validity detection module prior to algorithmic analysis. A 2D U-Net model was trained to evaluate image sharpness and assign a quality score to each section. Low-quality images were then reviewed using a custom annotation tool, allowing experts to determine whether re-acquisition or replacement was necessary, thereby enabling efficient quality control. To prevent artifacts from affecting downstream analysis, we further implemented CNN-based tissue mask generation. A U-Net model was trained on three manually annotated chunks (8,600 × 8,600 × 31 voxels at 32 × 32 × 33 nm^3 per voxels) to classify voxels into in-brain tissue, background, and defect regions (e.g., folds, tears). All predicted masks were manually reviewed to ensure accurate detection of artifact-prone areas. The resulting quality and tissue masks were applied throughout the processing pipeline for artifact exclusion and region-of-interest selection, substantially improving the reliability of segmentation and agglomeration results.

Image stitching and alignment

The 3D volume registration of EM images was accomplished through two sequential stages: tile stitching followed by section alignment. The stitching workflow proceeded through three computational stages: First, feature detection and matching using Scale-Invariant Feature Transform (SIFT) descriptors[70] extracted from tile overlap regions. Second, pairwise displacement estimation via coordinate transformation analysis. Third, global position optimization through linear least squares minimization. Specifically, SIFT-matched feature point pairs served as the basis for calculating local translation vectors between tiles. To mitigate error accumulation, a global optimization framework simultaneously adjusted all tile positions by minimizing the total displacement error across the entire section, thereby ensuring precise tile stitching within each section.

A multi-scale alignment method was implemented to register serial sections through coarse- and fine-scale processing. To address error accumulation, the pipeline employed a sub-volume-division strategy, partitioning the original dataset into 764 spatially coherent stacks (each containing 31 consecutive sections). Continuity across stacks was established by selecting the first section of each stack as a reference section (764 total). These references underwent affine transformation to correct notable deformations while maintaining spatial invariance throughout alignment, serving as stable pivots to prevent cumulative error propagation. Alignment then proceeded within each stack, from coarse to fine scales. Sections were downsampled 32-fold during coarse-scale alignment. Correspondences between two adjacent sections were initially extracted using

SIFT descriptors and subsequently filtered using the RANSAC algorithm[71] to enhance reliability. Affine transformation was applied to align adjacent sections. Sections were downsampled 8× during fine-scale alignment. Damaged sections were first aligned to their neighbors using an expected affine method[69]. Subsequently, an optimized elastic method[72] generated dense correspondence fields between adjacent sections, guiding the iterative refinement of deformation meshes that balanced local adaptability with global smoothness. Finally, Thin-Plate Spline (TPS) transformations[73] extrapolated these deformations to original-resolution sections, preserving ultrastructural continuity at synaptic resolution.

Bidirectional CLEM

To match the resolution of the template brain of the Zebrafish Mesoscopic Atlas (1 μm^3), the 764 reference sections were further downsampled in the xy-plane to generate downsampled whole-brain EM images (992 × 992 × 990 nm^3 per voxel) for bidirectional CLEM. Multimodal image registration was accomplished through a three-stage approach: First, whole-brain nuclei were extracted from both the Zebrafish Mesoscopic Atlas and ssEM datasets to create nuclei point clouds, which were then rigidly aligned using the Iterative Closest Point (ICP) algorithm[74]. Manually-annotated nuclei from four 6-dpf *Tg(HuC:H2B-GCaMP6f)* larvae were used to generate the average point cloud for the LM template brain, while nuclei from ssEM datasets were automatically segmented. Second, the EM images were globally constrained using X-ray data. Third, computed bidirectional deformation fields between LM and EM spaces through 3D template matching and TPS transformations. Somata regions across the entire central brain, along with other EM-identifiable brain regions including pineal gland, pituitary gland, and bilateral optic tectal neuropil regions, were manually annotated on downsampled whole-brain EM images for joint optimization. These annotated regions served as reference landmarks for registration with their well-established counterparts in the template brain of the Zebrafish Mesoscopic Atlas.

3D automatic reconstruction

Whole-brain 3D reconstruction was performed through an automated pipeline comprising: (1) image enhancement and denoising, (2) local registration, (3) chunk-based large-scale data prediction, (4) dense reconstruction, (5) intra-chunk agglomeration, and (6) chunk stitching.

To address the Poisson and Gaussian noise inherent in electron microscopy (EM) imaging and to overcome the challenges of self-supervised denoising with degraded inputs, we propose a novel framework, Blind2Unblind[75], for implicit lossless self-supervised denoising. This framework leverages a mask-guided medium to enhance and denoise EM images. It consists of a globally-aware mask mapper driven by mask-based sampling and a non-blind lossless training strategy based on re-visible loss. This denoising process provides high signal-to-noise ratio (SNR) and high-fidelity detail for subsequent brain neural atlas reconstruction and EM image analysis, ensuring the integrity and precision of the processed neural tissue slices.

In large-scale ssEM datasets, local misalignments caused by physical perturbations and sectioning inconsistencies can degrade segmentation accuracy, particularly for fine structures. To enhance local 3D continuity and improve inference performance, we adopted a chunk-based spatial registration strategy inspired

by the preprocessing pipeline of the Flood-Filling Network (FFN)[76]. For each chunk, a 4 × 4 affine transformation matrix was estimated to align it with a global reference space. Neural network inference, aggregation, and merging were then performed on the aligned chunks. After processing, inverse transformations were applied to map the results back to the original coordinate system, followed by cropping to restore the original dimensions. All affine matrices were precomputed and cached prior to processing to reduce computational overhead. This strategy improved boundary consistency and segmentation quality while significantly enhancing efficiency in large-scale data processing.

To efficiently process large-scale computational tasks, particularly for parallel neural network inference on high-volume datasets, we designed and implemented a distributed computing strategy based on spatial block partitioning. Specifically, the original three-dimensional volume was divided into a series of overlapping chunks to ensure boundary continuity and consistency in prediction. These chunks were then preprocessed and spatially realigned, and subsequently treated as independent inference tasks scheduled for parallel execution. The entire computational workflow was deployed on a high-performance distributed parallel computing architecture managed by the Slurm (Simple Linux Utility for Resource Management) workload manager. All sub-tasks were automatically submitted via batch scripts to a Slurm-managed HPC (High-Performance Computing Cluster) comprising more than 30 nodes. Based on the availability of computational resources, the scheduler dynamically distributed tasks across multiple physical nodes. Each node was equipped with a heterogeneous configuration of GPUs, including NVIDIA® A100, V100, and GeForce RTX 4090 models, thereby maximizing utilization of available hardware accelerators. Upon completion, the outputs of all sub-tasks were automatically aggregated and post-processed to reconstruct the full prediction results over the entire volume. For tasks including neuron, synapse, and mitochondria segmentation, the block and overlap sizes are set to 8,600 × 8,600 × 31 and 600 × 600 × 1 pixels, with a resolution of 4 × 4 × 33 nm^3. For tasks such as nucleus detection and vessel recognition, the block and overlap sizes are set to 1,075 × 1,075 × 31 and 75 × 75 × 1 pixels, with a resolution of 32 × 32 × 33 nm^3.

In this study, we employed a boundary detection-based dense segmentation approach to process the whole-brain zebrafish electron microscopy dataset. The image segmentation network adopts a U-shaped architecture with residual blocks, and is trained to predict nearest-neighbor affinity maps along all three spatial dimensions. The training dataset consists of seven randomly selected chunks, each comprising 30 consecutive sections with a spatial size of 2,000 × 2,000 × 30 voxels at a resolution of 4 × 4 × 33 nm^3. All chunks were manually annotated by domain experts. A composite loss function combining weighted cross-entropy and Dice loss was employed to enhance segmentation performance, particularly in the presence of class imbalance. To improve model generalization, we applied a range of data augmentation techniques during training, including basic transformations such as rotation, flipping, and elastic deformation, as well as robustness-oriented strategies such as CutBlur, CutNoise, and Mixup. In addition, we simulated common imaging artifacts—including registration shifts, motion blur, and partial slice dropouts—to enhance the model's ability to handle real-world imperfections, thereby improving the stability and accuracy of the segmentation.

To construct the signature graph, the first step involves over-segmentation of the membrane probability map using a 2D watershed algorithm based on distance transform. Specifically, small connected membrane

boundary components are removed through thresholding. Given the strong anisotropy of the data (with lateral resolution of 4 nm/pixel and axial resolution of 33 nm/pixel), the Euclidean distance transform is applied to each membrane probability map. The maximum distance value is then used as the seed point to execute the watershed algorithm, producing 2D watershed superpixels. These superpixels are subsequently merged to achieve the 3D reconstruction of the cell. The image can be represented at a more abstract level using watershed superpixels, where the superpixels serve as vertices and the physical connectivity between them forms the edges of a graph model. The superpixel merging problem is thus formulated as a vertex partitioning problem on the graph. In this study, the problem is modeled as the minimum cost multicut problem (MCMP) on the superpixel adjacency graph[77]. For feature extraction, three types of features are manually extracted: boundary features between superpixels, edge features within each superpixel, and inter-layer features derived from anisotropic data. A feature vector of length 625 is designed for each edge between two superpixels. A random forest classifier is then trained to predict the probability of merging each pair of superpixels. Based on maximum likelihood estimation, the predicted probability is converted into the cost for merging the two superpixels. This results in an instance of the multicut problem. Additionally, previously reconstructed and expert-verified whole-brain nucleus and synapse identification results are introduced as soft priors[78]. Superpixels belonging to the same nucleus should be merged preferentially, while superpixels on opposite sides of the same synapse should be merged less likely. At the same time, the aggregation range is confined to the effective tissue mask area to prevent the merging of defect regions with other superpixels, thereby avoiding erroneous propagation.

Given that the combinatorial optimization problem defined here is NP-hard, and exact methods are not polynomial-time solvable, this study frames the problem as a sequential decision-making task for node aggregation on the graph. The problem is solved optimally using the heuristic greedy additive edge contraction (GAEC) framework[79]. Finally, the results are mapped back to the original over-segmented image obtained from the watershed distance transform.

Following the preliminary reconstruction of all individual chunks, we developed an overlap-aware fragment agglomeration algorithm to accurately identify and merge neuronal segments across adjacent chunks, thereby enabling the reconstruction of globally continuous neuronal structures. This algorithm integrates a deep learning-based candidate identification module with a set of rule-based merging constraints. Specifically, we trained a 3D-ResNet-based neural network classifier to evaluate fragment pairs extracted from sliding 3D windows within overlapping regions, producing a probability score indicating whether the pair originates from the same neuron. Candidate merges were then further filtered based on multiple criteria, including intersection-over-union (IoU) thresholds, voxel overlap chunk, and the presence of defect masks, to ensure that the final agglomeration decisions maintain both structural continuity and biological plausibility. By combining large-scale parallel processing enabled by the Slurm workload manager with this customized post-processing pipeline, we established an efficient, scalable, and robust workflow for dense neuronal reconstruction, well-suited for automated analysis of ultra-large-scale 3D EM datasets in connectomics research.

Nucleus and vessel segmentation

We performed automatic reconstruction of structures such as cell nuclei and blood vessels. To expand the diversity of annotations under the constraint of limited labeling costs, we annotated every fifth section from the original whole-brain ssEM dataset, creating a subset with a resolution of 32 × 32 × 165 nm^3. This annotated data was used to train a 2D segmentation network, which, after multiple iterations, generated a high-quality training set with dimensions of 9,000 × 6,000 × 764 voxels. To ensure that the training and validation sets followed the same distribution, the original data was sampled at the same intervals, resulting in five test sets with resolutions consistent with the training set. We employed nnU-Net[80] for training and inference, with a patch size set to 1,024 × 1,024 × 4 and a batch size of 2. To maintain training stability, we chose stochastic gradient descent (SGD) with a momentum of 0.99 as the optimizer and applied a "poly" learning rate policy, starting with a learning rate of 0.01 and a maximum of 1,000 epochs. Upon completion of inference, we restored the test data to the original space, resulting in a coarse reconstruction of the entire volume. However, this approach still produced fragmented noise. To address this issue, we implemented a sliding window strategy along the z-axis, systematically traversing connected instances within each window. The window length was set to 30, with an overlap of 4. When the number of voxels within the receptive field was less than 1000, the z-axis voxel range was under 2, and the instance did not contact adjacent windows, we classified it as reconstruction noise and removed it. Ultimately, we achieved a refined reconstruction of the whole-brain nuclei and vessels. The automatic reconstructed results underwent manual proofreading, followed by quantitative analysis and 3D visualization.

Nucleus clustering

A comprehensive feature extraction pipeline was developed, integrating both traditional handcrafted morphological features and high-level representations learned through self-supervised learning, to analyze whole-brain nuclei with diverse morphologies. Manually-proofread nuclei supervoxels (n = 176,239; Nuclei with incomplete structures in rostral and caudal sections were excluded) were processed using the CloudVolume framework to compute 3D surface meshes and then extracted 15 traditional morphological features using the Trimesh library. These 15 features collectively characterize nucleus compactness (Φ, κ_A, κ_V), surface irregularity (ΔA, ΔA_b), shape elongation (ρ_{max}, R_{range}), and spatial dispersion (r_{max}, r_{min}). The following notation was adopted:

M: 3D triangular mesh representing a nucleus surface.

V: Volume of the nucleus mesh (μm^3).

A: Surface area of the nucleus mesh (μm^2).

C: Geometric centroid of the nucleus mesh.

M_h: Convex hull mesh of M.

V_h, A_h: Volume and surface area of convex hull, respectively.

S_b: Minimal bounding sphere of M.

V_b, A_b: Volume and surface area of bounding sphere, respectively.

v_i: i-th vertex of mesh M.

$\|\cdot\|$: Euclidean norm in $\mathbb{R}^3$.

Φ: Sphericity defined as $\Phi = \pi^{1/3}(6V)^{2/3}/A$, where $\Phi \in [0, 1]$ and $\Phi = 1$ defines a perfect sphere.

κ_A: Surface convexity defined as $\kappa_A = A/A_h$

κ_V: Volume convexity defined as $\kappa_V = V/V_h$

ΔA: Surface concavity defined as $\Delta A = A_h - A$

ΔV: Volume concavity defined as $\Delta V = V_h - V$

ρ_{max}: Elongation ratio defined as $\rho_{max} = \max_i(\|v_i - C\|)/\min_i(\|v_i - C\|)$

R_{range}: Radial range defined as $R_{range} = \max_i(\|v_i - C\|) - \min_i(\|v_i - C\|)$

r_{max}: Normalized max radius defined as $r_{max} = (\max_i(\|v_i - C\|))^3/V$

r_{min}: Normalized min radius defined as $r_{min} = (\min_i(\|v_i - C\|))^3/V$

σ_A: Spherical area ratio defined as $\sigma_A = A/A_b$

σ_V: Spherical volume ratio defined as $\sigma_V = V/V_b$

ΔA_b: Spherical surface excess defined as $\Delta A_b = A_b - A$

ΔV_b: Spherical volume excess defined as $\Delta V_b = V_b - V$

To complement these interpretable, handcrafted features, a self-supervised deep learning framework was implemented to extract high-level geometric representations of the nucleus shape. Unlike voxel- or mesh-based formats, point clouds provide a compact and resolution-independent representation that preserves fine morphological details. Each nucleus surface mesh M was uniformly sampled using Poisson disk sampling in Trimesh to obtain a point cloud $P \in \mathbb{R}^{n\times 3}$, where n = 3,072 represents the number of sampled vertices. The sampling process ensures uniform spatial distribution across the mesh surface while preserving geometric details. The point clouds were processed using a Siamese self-supervised architecture based on SimSiam[81] to learn transformation-invariant descriptors. Let P denote the input point cloud. During training, each point cloud was augmented into two distorted views P_1 and P_2 using random rotations, Gaussian noise, and jittering. The augmented views were processed through a three-stage neural network pipeline:

$$f: \mathbb{R}^{n\times 3} \rightarrow \mathbb{R}^{d} \rightarrow g: \mathbb{R}^{d} \rightarrow \mathbb{R}^{d'} \rightarrow h: \mathbb{R}^{d'} \rightarrow \mathbb{R}^{d'}$$

where $f(\cdot)$ (Encoder network, PointNet-based backbone) maps point clouds to d = 1,024-dimensional embeddings, $g(\cdot)$ (Projector network, 2-layer MLP) maps to d' = 256-dimensional projections, and $h(\cdot)$ (Predictor network, 2-layer MLP) with same dimensionality. The model was trained to minimize a symmetric negative cosine similarity loss:

$$\mathcal{L} = -\tfrac{1}{2}[D(h(g(f(P1))), \underline{g(f(P2))}) + D(h(g(f(P2))), \underline{g(f(P1))})]$$

where $D(x, y) = x\cdot y/(\|x\|_2 \|y\|_2)$ denotes the cosine similarity function. The underlined terms are treated as constants during backpropagation and do not contribute gradients. This objective encourages the network to learn rotation- and noise-invariant representations while preventing representational collapse. Each nucleus was ultimately represented by a d = 1,024-dimensional embedding vector $z = f(P)$ extracted from the trained encoder. To reduce redundancy and enable integration with handcrafted features, we applied Uniform Manifold Approximation and Projection (UMAP)[82] with the following hyperparameters (Target dimensionality: d_{UMAP} = 8; Number of neighbors: k = 15; Minimum distance: d_{min} = 0.1; Distance metric: Euclidean). This yielded an 8-dimensional deep feature representation $z_{UMAP} \in \mathbb{R}^8$ for each nucleus. The final feature representation for each nucleus was constructed by concatenating the 8-dimensional deep feature embedding $z_{UMAP} \in \mathbb{R}^8$ with the 15-dimensional handcrafted morphological feature vector $f_{morph} \in \mathbb{R}^{15}$: $f_{hybrid} = [f_{morph}; z_{UMAP}] \in \mathbb{R}^{23}$, where $[\cdot; \cdot]$ denotes vector concatenation. Prior to concatenation, all features

were standardized using z-score normalization: $f' = (f - \mu)/\sigma$, where μ and σ represent the mean and standard deviation computed across the entire dataset, respectively. This hybrid descriptor f_{hybrid} leverages both interpretable morphological traits (providing biological insight) and high-capacity deep embeddings (capturing complex geometric patterns), enabling robust and scalable analysis of nucleus morphology.

PSD, SV, and mitochondria segmentation

A three-class 3D U-Net was trained to predict the synaptic clefts and vesicle clouds at the resolution of 8 × 8 × 33 nm^3. Ground truth data was generated by four manually annotated regions (~12 × 12 × 1 μm^3 per volume), undergoing multiple rounds of expert verification and encompassing 146M voxels. We optimized the network using the multi-class cross-entropy loss and SGD optimizer. During training, a warm-up learning rate strategy was employed with an initial learning rate of 0.01, a linear warm-up period of 2k steps, and cosine decay over a total of 500k training steps.We also conducted data augmentation to improve the network's robustness, including random rotation, random flipping, grayscale transformation, elastic transformation, and blur simulation. To test the network performance, we manually annotated another three regions as test sets (~8 × 8 × 1 μm^3 per volume). The evaluation of these regions yielded an average precision of 85.60 ± 3.205% and an average recall of 88.37 ± 1.593%.

A 3D U-Net was trained to detect the mitochondria at the resolution of 8 × 8 × 33 nm^3. Ground truth data was generated by five manually annotated regions (~12 × 12 × 1 μm^3 per volume), undergoing multiple rounds of expert verification and encompassing 467M voxels. To separate adjacent mitochondria, we designed a network to simultaneously predict both a mitochondrial mask (trained with binary cross-entropy loss) and an instance boundary mask (optimized using a combined binary cross-entropy and Dice loss). Training proceeded for 500k iterations with SGD optimizer, applying a learning rate scheduling strategy identical to the synapse detection task. Data augmentation protocols were consistently implemented as in the synapse detection framework. For automated identification of glycinergic neurons, we annotated additional 284 soma-localized mitochondria labeled with APEX2. Neurons were classified as glycinergic if their somata contained ≥ 4 labeled mitochondria.

Proofreading

Extensive manual and semi-automated proofreading of the multi-scale segmentation improved the accuracy of the neural circuit reconstruction. The Advanced Connectome Engine (ACE) is a custom-built software designed for reconstructing large-scale neural data, integrating massive data management, intelligent computing, and collaborative tools. The Hadoop- and HBase-based data management system enables the deployment of elastic, secure distributed clusters for storing and rapidly retrieving large-scale connectome data, including ssEM images and reconstruction results. In the proofreading system, reconstruction results are represented as graph structures that connect segmentation contours across all serial sections belonging to a single supervoxel. This data structure enhances proofreading efficiency by enabling comparison of adjacent layer contours to identify anomalies in reconstructions and guide proofreaders to target regions requiring correction. To streamline proofreading project oversight and ensure quality control, we integrated a project management module into the system. This module centrally coordinates proofreading tasks, facilitates

collaborative proofreading workflows, and logs all user operations and comparisons between current and immediately preceding proofreading results, enabling real-time monitoring of proofreader performance metrics. The proofreading team consisted of 30 – 40 full-time proofreaders from commercial companies and several experts from our laboratories.

Notably, we utilized a series of foundation models for segmentation, specifically the Segment Anything Model (SAM), SAM 2 and SAEM², to aid our proofreading workflow[83-85]. Based on these models, we implemented two additional strategies to enhance our software's human-computer interaction: (1) The SAM ViT-H model checkpoint was exported to an ONNX (Open Neural Network Exchange) model with additional quantization and optimization. ONNX Runtime was used to execute these models on CPU/GPU, which supported cross-platform inference and improved software runtime. (2) The SAM embeddings generated by encoders were precomputed and saved in CloudVolume using kempressed format, which demonstrated higher compression ratios compared to raw and fpzip encodings. For 2D semi-automated segmentation, we utilized manually traced neuronal skeletons with extra positive/negative points as input prompts for the SAM model. However, the pretrained SAM fail to accurately segment densely packed, homogeneous neuronal processes[86]. To address this, we proposed the finetuned SAEM² with auxiliary tasks to acquire complementary multi-head information for neuron segmentation in ssEM datasets. Here, the auxiliary task involved identifying cell boundaries (plasma membranes) to complement the original SAM, which primarily focuses on cell masks. For 3D segmentation, we employed the SAM 2 augmented with two additional strategies: (1) We trained the system to predict cross-correlation maps and subsequently computed the shifts between adjacent 2D EM images. (2) We utilized the distance transformation maps from the previous cell masks to sample prompt points for generating the next cell masks.

Micro-mesoscopic skeleton matching

Upon comparing the neuronal skeletons with those in the Zebrafish Mesoscopic Atlas, which molecularly defined types are known, we inferred the putative types (primarily glutamatergic/excitatory or GABAergic/inhibitory) of APEX2-negative neurons based on morphological similarity. A preprocessed reference file was generated, containing the x-y-z coordinates of all excitatory/inhibitory (E/I) neurons and their mirrored counterparts from the Zebrafish Mesoscopic Atlas ($n_{vglut2a/2b}$ = 12,219, n_{gad1b} = 5,371, n_{glyt2} = 2,193). We first calculated neuronal skeletons (stored as swc files) from manually-corrected EM supervoxels. These skeletons were then transformed into the common physical space of the mesoscopic brain template using bidirectional CLEM. Using the soma center of EM skeletons (manually annotated during proofreading) as the origin, we retrieved all single-neuron morphological data within a 25 μm spherical radius based on the preprocessed reference file. For each EM skeleton, we performed pairwise morphology comparisons with the retrieved mesoscopic skeletons. Cross-scale skeleton matching establishes morphological correspondences between the same type of neurons across imaging modalities by quantifying spatial relationships between their reconstructed skeletons. Mesoscopic datasets provide a complete neuronal skeleton (S_L), and incompletely reconstructed microscopic datasets yields only a partial skeleton (S_E). Therefore, S_E is set as the reference, and the matching similarity is constructed by calculating the unidirectional distance to S_L. Specifically, the distance D between S_L and S_E is calculated as follows:

$$D=\frac{1}{|S_E|}\sum_{p\in S_E} D_{min}(p,S_L)$$

where D_{min} represents the shortest distance from S_L to the point p in S_E. The distance for each point in S_E is calculated, and the average is then determined. The S_L that minimizes D is chosen as the most similar skeleton corresponding to S_E. This distance-based scoring system ranks similarity (lower scores indicate closer matches), with the top 10 matches (swc filenames and scores) exported per EM skeleton. Manual verification was performed to both validate the matching accuracy and determine the E/I identity of EM-reconstructed neurons. These functions have been integrated into our open-source, all-in-one framework Brain Atlas Viewer (BrAVe), which unifies multimodal data to facilitate seamless micro-mesoscopic data integration.

3D Visualization

In accordance with open-science principles, we employed the Neuroglancer precomputed format and CloudVolume interface for data management and 3D visualization through both Neuroglancer and webKnossos[87]. For data encoding, we used JPEG compression for ssEM images and compressed_segmentation format for region silhouettes and segmentation masks. We further implemented the Igneous[88] for multiprocessed block-wise downsampling, skeletonization and meshing with the following agglomeration. For skeletonization, we used the Kimimaro implementation of the automated TEASAR[89] algorithm. We then merged the skeleton splits that may appear based on nearest Euclidean neighbors, calculated the path length of the skeleton, and determined the radius of each vertex in the skeleton. For meshing, we used the automated block-wise Zmesh to generate multi-resolution meshes. These skeletons and meshes were stored in sharded formats.

We employed mesh representations to visualize brain regions and reconstructions in Neuroglancer, while utilizing annotation points to demonstrate synaptic locations. The Neuroglancer *matrix* function served as an affine transformation tool for manipulating (translate/flip/rotate/zoom) the original image layers. We used the parallel projection during Neuroglancer rendering to generate 3D scale bars. Furthermore, We optimized two existing workflows for video creation: (1) the Neuroglancer workflow using Python scripts from the *video_tool* package, and (2) the open-source computer graphics software Blender, with Python scripts and JSON descriptions from neuVid. Notably, since we acquired high-resolution images only for the brain, unilateral retina, and unilateral optic nerve, we processed a pre-acquired low-resolution (~0.4 × 0.4 × 1.65 μm^3 per voxel) dataset of the complete zebrafish head to provide comprehensive 3D rendering context used in **Fig.1b**. This data was first manually verified against the whole brain section number corresponding to each image. The subsequent processing included interpolation, registration with high-resolution images, and grayscale histogram equalization. Our ssEM data are publicly accessible through the following dedicated links:

Brain EM images, https://ng.zebrafish.digital-brain.cn/Fish-X/Brain_EM_images

Retina EM images, https://ng.zebrafish.digital-brain.cn/Fish-X/Retina_EM_images

Brain regions, https://ng.zebrafish.digital-brain.cn/Fish-X/Brain_regions

Auto-reconstructed supervoxels, https://ng.zebrafish.digital-brain.cn/Fish-X/Auto_supervoxels

Manual-corrected neurons, https://ng.zebrafish.digital-brain.cn/Fish-X/Manual_supervoxels
Manual-corrected nuclei, https://ng.zebrafish.digital-brain.cn/Fish-X/Nuclei
Manual-corrected vessel, https://ng.zebrafish.digital-brain.cn/Fish-X/Vessel

Statistical analysis

Kolmogorov-Smirnov test was used for testing normality. Mann Whitney U test was used in Fig. 2d, 3k, 4d,e. Paired t test was used in Fig.4g,h. $^{*}P < 0.05$, $^{**}P < 0.01$, $^{***}P < 0.001$.

Acknowledgement

We are grateful to Xu-long Wen, Xin-peng Shi, Xiao-tong Sun, Ning Wang, Ying Wang, and other staffs from Grand View (Beijing) Technology Co., Ltd, Zhi Zeng, Le Wang, Xian-wei Cao, Lang Zhang, Wan Deng, Xing-yang Du, Yu-ran Liu, and other staffs from Chengdu Huizhong Tianzhi Tech. Co., Ltd. (www.hztzai.com) for massive manual proofreading and management, Dr. Yu Kong, Dr. Xu Wang, Li-jun Pan, Xue Xu for assistance in sample preparation, Drs. Ke Zhang, Yun-feng Hua, Jun Zhang, Dan-qian Liu, Yu Mu, Kai Yang, and Sheng-xiong Wang for insightful advice on sample preparation and research direction, the Transdisciplinary Platform of Functional Connectome and Brain-inspired Intelligence in Huairou Science City in Beijing and the Microscopic Technology & Analysis Center at the Institute of Automation, Chinese Academy of Sciences for providing technical support and device resources, Dr. Jie He for providing the *TgBAC(gad1b:GAL4-VP16)*, Dr. Misha Ahrens for providing the *Tg(HuC:H2B-GCaMP6f)*, Dr. Koichi Kawakami for providing *Tg(UAS:GCaMP6s)*, *Tg(5×UAS-TATA:EGFP)* and *Gt(vmat2:GAL4FF)*, Dr. Joe Fetcho for providing the *Tg(glyt2:GFP)*, Ming-quan Chen, Hong-li Wan and other staffs from Facility of Mapping Brain-Wide Mesoscale Connectome (FMBWMC) for assistance in utilizing the Zebrafish Mesoscopic Atlas and BrAVe, Ting-ting Zhao and Yong-wei Zhong from FMBWMC for initial quality assessment of automated segmentation results, Jia-wen Huang, Liu-qin Qian, Chen-xi Jin and other staffs from the Big Data of Brain Atlas Facility for establishing a web-sharing platform, Dr. Qian Hu for optical imaging and image processing support, Dr. Chun-feng Shang, Dr. Rong-wei Zhang, Dr. Jia Li, Dr. Yu-fan Wang, Dr. Sha Li, Dr. Le Sun, Dr. Qiu-sui Deng, Li-jun Chen for progress discussions, Ji-wen Bu for daily laboratory operations management, and Ye Hua, Shi-rong Jin, Ning-xin Ren for Fish Facility management. This work was supported by National Science and Technology Innovation 2030 Major Program of the Ministry of Science and Technology (2021ZD0204500, 2021ZD0204502 and 2021ZD0204503), Creative Research Groups (32321003) and general grant (32171461) of the National Natural Science Foundation of China, Shanghai Municipal Science and Technology Major Project (18JC1410100 and 2018SHZDZX05), and Key Research Program of Frontier Sciences (QYZDYSSW-SMC028) and Strategic Priority Research Program (XDB32010200) of Chinese Academy of Sciences.

Author contributions

J.D. and H.H. conceived and supervised the project. F.L. generated APEX2-labeled fish lines, prepared EM samples, organized proofreading and daily discussions, and drafted the manuscript. J.L. performed the automatic reconstruction of this ssEM dataset, including nucleus and vessel segmentation. C.S. generated

APEX2-labeled fish lines, prepared EM samples, analyzed the input organization of the LC-NE system, and was responsible for fish line management. J.Y. and L.S. were responsible for proofreading system maintenance and data management. Y.L. and X.C. performed image alignment and CLEM. J.L. performed the automatic segmentation of PSD, SV, and mitochondria. L.Z. was responsible for image acquisition. L.L. collected all ultrathin sections. H.Z. conducted skeletonization and 3D visualization. B.C. handled image denoising and enhancement. Y.Z. executed nucleus clustering. H.C., S.C., and F.Z. participated in image alignment. J.G. participated in vessel segmentation. H.Y. and J.Z. carried out micro-mesoscopic skeleton comparison. H.M. performed ion milling. T.X. was responsible for wrinkle restoration. X.D. assisted in section collection. L.L. contributed to image acquisition. X.Z. supported remote proofreading management. Q.X. participated in reconstruction. Z.F. and Y.W. participated in proofreading. C.Z., P.X., and Y.Y. conducted functional investigations of the LC-NE system. Y.Q. and Y.G. participated in progress discussions. X.D. supported the utilization of the Zebrafish Mesoscopic Atlas and BrAVe.

Competing interests

The authors declare no conflict of interest.

References

56. Chen Q, Jiang L, Li C, et al. Haemodynamics-driven developmental pruning of brain vasculature in zebrafish. *PLoS Biol*. 2012;10(8):e1001374. doi:10.1371/journal.pbio.1001374
57. McLean DL, Fan J, Higashijima S, et al. A topographic map of recruitment in spinal cord. *Nature.* 2007;446(7131):71-75. doi:10.1038/nature05588
58. Prober DA, Rihel J, Onah AA, et al. Hypocretin/orexin overexpression induces an insomnia-like phenotype in zebrafish. *J Neurosci*. 2006;26(51):13400-13410. doi:10.1523/JNEUROSCI.4332-06.2006
59. Asakawa K, Suster ML, Mizusawa K, et al. Genetic dissection of neural circuits by Tol2 transposon-mediated Gal4 gene and enhancer trapping in zebrafish. *Proc Natl Acad Sci U S A*. 2008;105(4):1255-1260. doi:10.1073/pnas.0704963105
60. Quirin S, Vladimirov N, Yang CT, et al. Calcium imaging of neural circuits with extended depth-of-field light-sheet microscopy. *Opt Lett*. 2016;41(5):855-858. doi:10.1364/OL.41.000855
61. Muto A, Lal P, Ailani D, et al. Activation of the hypothalamic feeding centre upon visual prey detection. *Nat Commun*. 2017;8:15029. doi:10.1038/ncomms15029
62. Li J, Zhang BB, Ren YG, et al. Intron targeting-mediated and endogenous gene integrity-maintaining knockin in zebrafish using the CRISPR/Cas9 system. *Cell Res*. 2015;25(5):634-637. doi:10.1038/cr.2015.43
63. Shang CF, Wang YF, Zhao MT, et al. Real-time analysis of large-scale neuronal imaging enables closed-loop investigation of neural dynamics. *Nat Neurosci*. 2024;27(5):1014-1018. doi:10.1038/s41593-024-01595-6
64. Kawakami K. Tol2: a versatile gene transfer vector in vertebrates. *Genome Biol*. 2007;8 Suppl 1(Suppl 1):S7. doi:10.1186/gb-2007-8-s1-s7
65. Ariotti N, Hall TE, Rae J, et al. Modular Detection of GFP-Labeled Proteins for Rapid Screening by

Electron Microscopy in Cells and Organisms. *Dev Cell*. 2015;35(4):513-525. doi:10.1016/j.devcel.2015.10.016

66. Martell JD, Deerinck TJ, Lam SS, Ellisman MH, Ting AY. Electron microscopy using the genetically encoded APEX2 tag in cultured mammalian cells. *Nat Protoc*. 2017;12(9):1792-1816. doi:10.1038/nprot.2017.065
67. Hua Y, Laserstein P, Helmstaedter M. Large-volume en-bloc staining for electron microscopy-based connectomics. *Nat Commun*. 2015;6:7923. doi:10.1038/ncomms8923
68. Willingham MC, Rutherford AV. The use of osmium-thiocarbohydrazide-osmium (OTO) and ferrocyanide-reduced osmium methods to enhance membrane contrast and preservation in cultured cells. *J Histochem Cytochem*. 1984;32(4):455-460. doi:10.1177/32.4.6323574
69. Xin T, Shen L, Li L, et al. Expected affine: A registration method for damaged section in serial sections electron microscopy. *Front Neuroinform*. 2022;16:944050. doi:10.3389/fninf.2022.944050
70. Lowe, D.G. Distinctive image features from scale-invariant keypoints. *International Journal of Computer Vision*. 2004;60(91-110). doi:10.1023/B:VISI.0000029664.99615.94
71. Fischler MA, Bolles RC. Random sample consensus: a paradigm for model fitting with applications to image analysis and automated cartography. *Comm. of the ACM,*. 1981;24(381-395). doi:10.1145/358669.358692
72. Saalfeld S, Fetter R, Cardona A, et al. Elastic volume reconstruction from series of ultra-thin microscopy sections. *Nat Methods*. 2012;9(7):717-720. doi:10.1038/nmeth.2072
73. Duchon, J. (1977). Splines minimizing rotation-invariant semi-norms in Sobolev spaces. In: Schempp, W., Zeller, K. (eds) Constructive Theory of Functions of Several Variables. Lecture Notes in Mathematics, vol 571. Springer, Berlin, Heidelberg. doi:10.1007/BFb0086566
74. Paul J Bes, Neil D McKay, et al. A method for registration of 3-d shapes. *IEEE Transactions on Pattern Analysis and Machine Intelligence*. 1992;14(2):239-256. doi:10.1109/34.121791
75. Wang Z, Liu J, Li G, et al. Blind2unblind: Self-supervised image denoising with visible blind spots. *Proceedings of the IEEE/CVF conference on computer vision and pattern recognition*. 2022: 2027-2036
76. Januszewski M, Kornfeld J, Li PH, et al. High-precision automated reconstruction of neurons with flood-filling networks. *Nat Methods*. 2018;15(8):605-610. doi:10.1038/s41592-018-0049-4
77. Beier T, Pape C, Rahaman N, et al. Multicut brings automated neurite segmentation closer to human performance. *Nat Methods*. 2017;14(2):101-102. doi:10.1038/nmeth.4151
78. Hong B, Liu J, Shen L, et al. Graph partitioning algorithms with biological connectivity decisions for neuron reconstruction in electron microscope volumes[J]. Expert Systems with Applications, 2023, 222: 119776.
79. Keuper M, Levinkov E, Bonneel N, et al. Efficient decomposition of image and mesh graphs by lifted multicuts. *Proceedings of the IEEE international conference on computer vision*. 2015: 1751-1759
80. Isensee F, Jaeger PF, Kohl SAA, et al. nnU-Net: a self-configuring method for deep learning-based biomedical image segmentation. *Nat Methods*. 2021;18(2):203-211. doi:10.1038/s41592-020-01008-z
81. Chen, X., & He, K. (2021). Exploring simple siamese representation learning. In Proceedings of the IEEE/CVF Conference on Computer Vision and Pattern Recognition (pp. 15750-15758)

82. McInnes, L., Healy, J., & Melville, J. (2018). UMAP: Uniform manifold approximation and projection for dimension reduction. arXiv preprint arXiv:1802.03426
83. Kirillov, A., Mintun, E., Ravi, N., et al. (2023). Segment Anything. IEEE International Conference on Computer Vision, 3992–4003. https://doi.org/10.1109/ICCV51070.2023.00371
84. Ravi, N., Gabeur, V., Hu, Y.-T., et al. (2024, October 4). SAM 2: Segment Anything in Images and Videos. The Thirteenth International Conference on Learning Representations. https://openreview.net/forum?id=Ha6RTeWMd0
85. Zhai H, Guo J, Zhang Y, et al. (2024). SAvEM3: Pretrained and distilled models for general-purpose 3D neuron reconstruction. 2024 IEEE International Conference on Bioinformatics and Biomedicine (BIBM), 3972–3977. https://doi.org/10.1109/bibm62325.2024.10822494
86. Januszewski, M., & Jain, V. Next-generation AI for connectomics. *Nat Methods*. 2024;21(8):1398-1399. https://doi.org/10.1038/s41592-024-02336-0
87. Boergens, K. M., Berning, M., Bocklisch, T., Bräunlein, D., Drawitsch, F., Frohnhofen, J., Herold, T., Otto, P., Rzepka, N., Werkmeister, T., Werner, D., Wiese, G., Wissler, H., & Helmstaedter, M. (2017). webKnossos: efficient online 3D data annotation for connectomics. Nature Methods, 14(7), 691–694. https://doi.org/10.1038/nmeth.4331
88. Silversmith, W., Zlateski, A., Bae, J. A., Tartavull, I., Kemnitz, N., Wu, J., & Seung, H. S. (2022). Igneous: Distributed dense 3D segmentation meshing, neuron skeletonization, and hierarchical downsampling. Frontiers in Neural Circuits, 16, 977700. https://doi.org/10.3389/fncir.2022.977700
89. Sato, M., Bitter, I., Bender, M. A., Kaufman, A. E., & Nakajima, M. (2002). TEASAR: tree-structure extraction algorithm for accurate and robust skeletons. Proceedings the Eighth Pacific Conference on Computer Graphics and Applications, 281–449. https://doi.org/10.1109/pccga.2000.883951

1225 **Figure Legends**

1226 **Fig. 1 | Multiplexed NM-type-labeled whole-brain ssEM of larval Zebrafish. a,** Schematic diagram of
1227 multiplexed EM labeling using APEX2-labeled larvae. Subcellular-localized APEX2 catalyzes the conversion
1228 of DAB into osmiophilic substances, creating localized, non-transmembrane electron densities within specific
1229 neuronal types and generating distinct EM-visible patterns. **b,** Rendering of the intact larval brain from this
1230 study (992 × 992 × 660 nm^3 per voxel resolution) was generated from pre-acquired EM images (~400 × 400 ×
1231 1,650 nm^3 per voxel resolution), which were processed using linear interpolation, registration to
1232 high-resolution whole-brain ssEM data, and grayscale equalization. Manually corrected brain-wide vessels
1233 (red) and neuronal tracts (yellow) are shown simultaneously. Representative EM images of the optic nerve
1234 (top-right) and retina (bottom-right) in coronal section are shown. **c,** Rendering of manually corrected
1235 brain-wide vessels (red) and neuronal tracts (yellow). Most vessels remained well-preserved, though some
1236 collapse was observed in telencephalon. Vessels were automatically reconstructed, followed by manual
1237 proofreading. Neuronal tracts, identified as a bundle of parallel-oriented fibers, were manually traced. **d,**
1238 Color-coded nuclear projection density along three axes. In the brain, 176,810 nuclei that were automatically
1239 segmented and subsequently manually proofread were used for analysis. Color-coded frequency distribution
1240 maps of nuclei along left-right (top), dorsal-ventral (top-left), and rostral-caudal (bottom-left) are shown. **e,**
1241 Rendering of all nuclei distributed across four representative horizontal planes along dorsal-ventral axis
1242 (interval: 50 μm). Z represents the dorsoventral distance relative to the epidermal surface. **f,** Rendering of
1243 incomplete reconstructions of brain-wide 533 manually-proofread neurons from this study. This includes
1244 retinal ganglion cells (RGC, n = 3), noradrenergic neurons in locus coeruleus and medulla oblongata (orange;
1245 $n_{LC\text{-}NE}$ = 12; $n_{MO\text{-}NE}$ = 2), dopaminergic neurons in olfactory bulb, posterior tuberculum, and caudal
1246 hypothalamus (light green; $n_{OB\text{-}DA}$ = 2; $n_{PT\text{-}DA}$ = 4; $n_{Hc\text{-}DA}$ = 2), serotonergic neurons in pretectum and superior
1247 raphe (dark blue; $n_{Pr\text{-}5HT}$ = 2; $n_{SR\text{-}5HT}$ = 4), hypocretinergic/orexinergic neurons in hypothalamus (purple; n_{Hcrt} =
1248 2), glycinergic neurons in hindbrain (sky blue; n_{Gly} = 22), several presynaptic partners of several
1249 monoaminergic neurons, and one Mauthner cell (white). Scale bars, 20 μm (panel **b**, optic nerve), 50 μm
1250 (panels **b,c,f**), 100 μm (panel **e**), 2% (panel **d**, frequency distribution). C, caudal; L, left; V, ventral; LC, locus
1251 coeruleus; MO, medulla oblongata; OB, olfactory bulb; PT, posterior tuberculum; Hc, caudal hypothalamus;
1252 SR, Superior raphe; Pr, pretectum; NE, noradrenergic; DA, dopaminergic; 5HT, serotonergic; Hcrt,
1253 hypocretinergic; Gly, glycinergic. See also Extended Data Figs. 1,2.

1254

1255 **Fig. 2 | Genetic labeling- and Mesoscopic Atlas-based neuron classification. a,** Schematic diagram of
1256 multi-strategy approaches for neuron classification. **b,** Representative EM images of all APEX2-labeled
1257 neuronal types (left) and their corresponding coronal sections (right). Individual labeled neurons are marked
1258 by white asterisks. Red boxes in right panels indicate the region shown in left panels. **c,** Rendering of a single
1259 LC-NE neuron's perisomatic ultrastructures, including nucleus (light green), nucleolus (red), endoplasmic
1260 reticulum (ER, orange), Golgi apparatus (pink), mitochondria (light blue), and a primary cilia.The
1261 mitochondria (top-right) and the ER (bottom-right) are depicted separately within the somatic contour. **d,**
1262 Within the LC region, comparisons of nuclear-to-cytoplasmic volume ratio and somatic mitochondrial density
1263 between APEX2-labeled NE neurons (orange; n = 5) and adjacent unlabeled cells (gray; n = 69). The blue

arrow points to an unlabeled cell with properties very similar to those of LC-NE neurons, which is speculated to be an unlabeled LC-NE neuron. $^{*}P < 0.05$, $^{***}P < 0.001$ (Mann Whitney U test). **e,** UMAP visualization of clustering of all cells in panel **d** using combined deep-learned and traditional features of their nuclei and somata. **f,** Rendering of five APEX2-labeled and the putative LC-NE neuron in panel **d**. Among these, partial axonal reconstruction was performed for LC-NE #3 and the putative LC-NE neuron, revealing similar projection patterns. **g,h,** Representative examples of partially EM-reconstructed neurons (black) paired with their fully LM-reconstructed excitatory (magenta, panel **g**) or inhibitory (sky blue and green, panel **h**) counterparts. The E/I identities of the top 10 candidates are displayed, with the best-matched neuron and highest-ranking non-matched type neuron indicated by color-coded arrowheads, respectively (bottom-left). 491 partially EM-reconstructed presynaptic neurons of the LC-NE system, previously registered to the mesoscopic brain template, were used as the query. All E/I neurons and their mirrored counterparts from the Zebrafish Mesoscopic Atlas ($n_{vglut2a/2b}$ = 12,219, magenta; n_{gad1b} = 5,371, sky blue; n_{glyt2} = 2,193, green) were used as the reference. **i,** The relationship between the minimum penalty score and the score difference separating the best-matched neuron from the highest-ranking non-matched type neuron. Among the 491 EM-reconstructed neurons, 342 exhibited mixed E/I profiles in their top-10 candidates (color-coded dots), while the remaining 149 showed exclusively excitatory or inhibitory candidates in their top-10 matches. Corresponding neurons in panel **g,h** are indicated by color-coded arrows. Lower penalty scores indicate higher degrees of matching. Greater differences suggest increased separability, indicating that excitatory and inhibitory neurons near EM queries display more distinct morphologies. **j,** Dual validation confirming the glycinergic identity of neuron #41 (white asterisk) in panel **h**. Upon comparing the micro-mesoscopic skeleton, this neuron was identified as a glycinergic neuron. Additionally, this neuron displayed glycinergic-specific mitochondrial APEX2-labeling, as indicated by the white arrows. Scale bars, 1 μm (panel **b**, expanded images), 5 μm (panels **c,j**), 50 μm (panel **b**, brain sections; panel **f**), Ro, rostral; L, left; V, ventral. ER, endoplasm reticulum; GA, Golgi apparatus; Mito, mitochondria. See also Extended Data Figs. 3,4; Supplementary Table 1,2.

Fig. 3 | Region- and neuron type-specific synaptic heterogeneity. a, The co-occurrence of PSDs (25.25 million), SVs (15.77 million), and mitochondria (13.73 million) in the brain. Automatic 3D reconstructed supervoxels were utilized to assess whether PSDs, SVs, and mitochondria are situated within the same presynaptic compartments. 56.6% of PSDs co-occurred with SVs and mitochondria, which were identified as typical synapses. **b,** Synapse density distribution across 52 major brain regions in the brain. 23.62 million synapses were identified based on the co-occurrence of PSDs and SVs. Mitochondria were not taken into account. Regions were ranked by synaptic density in descending order, with specific annotations for NL, OB, and PL. **c,** Linear regression analysis of synapse density versus nucleus density across whole-brain regions. The solid black line represents the fitted regression line ($Y = -173.3 \times X + 1{,}549$; $R^2 = 0.7070$, $P < 0.0001$, $n_{region} = 52$). Dashed black lines indicate the 95% confidence interval of the fit. Each circle represents an individual brain region. **d,** Lognormal distribution of the volume of synaptic components, including PSDs, SVs, and mitochondria, across various brain regions. The volume was calculated using the results of automatic segmentation. **e,f,g,** Lognormal distribution of the probability density for the volumes of PSDs

1303 (panel **e**), SVs (panel **f**), and mitochondria (panel **g**) across whole-brain regions. **h,i,** Rendering of EM
1304 reconstructions for multiple APEX2-labeled neurons. The overall distribution within the whole brain (panel **h**)
1305 and detailed morphologies (panel **i**), including synaptic input sites, are shown respectively. Several types of
1306 NM neurons, including NE neurons in the LC and MO (orange), DA neurons in the PT, OB, and Hc (light
1307 green), 5HT neurons in the SR and Pr (blue), peptidergic Hcrt neurons (magenta), and inhibitory glycinergic
1308 neurons (cyan), were reconstructed within the right hemisphere, with their dendritic input sites marked by
1309 small violet dots. Most of the reconstructions were situated within somatodendritic areas. Neuron counts are
1310 shown in parentheses. **j,** Rendering of the right Mauthner cell's soma, lateral dendrites, and ventral dendrites
1311 (gray), as well as somatodendritic synaptic input sites (small violet dots; $n_{synapse}$ = 1,966). The axonal branch
1312 in the upper right is not fully displayed. **k,** Comparison of dendritic input densities across various neuronal
1313 types. Dendrites were manually identified based on the localization of synaptic inputs. LC-NE neuron #3
1314 exhibits the highest number of synaptic inputs (n = 560), with the majority of its presynaptic neurons
1315 proofread for the analysis in Fig. 4. Dendritic input density (in per μm): LC-NE, 0.3493 ± 0.0194, n = 5;
1316 MO-NE, 0.1511 ± 0.0185, n = 3; PT-DA, 0.3420 ± 0.0212, n = 4; OB-DA, 0.0255 ± 0.0094, n = 3; Hc-DA,
1317 0.0415 ± 0.0249, n = 3; SR-5HT, 0.3749 ± 0.0413, n = 4; Pr-5HT, 0.0759 ± 0.0249, n = 3; Hcrt, 0.0747 ±
1318 0.0204, n = 2; Gly, 0.1318 ± 0.0163, n = 18. $^{*}P < 0.05$ (Mann Whitney U test). Error bars represent mean ±
1319 SEM. Scale bars, 15 μm (panel **i**), 50 μm (panel **h**). Ro, rostral; C, caudal; L, left; V, ventral; PSDs,
1320 postsynaptic densities; SVs, synaptic vesicles; Mito, mitochondria; OB, olfactory bulb; P, pallium; S,
1321 subpallium; Po, preoptic region; OTAOS, optic tract and accessory optic system; Pr, pretectum; E, epiphysis;
1322 Ha, habenula; DT, dorsal thalamus; VT, ventral thalamus; PT, posterior tuberculum; M2, migrated posterior
1323 tubercular region; Hr, rostral hypothalamus; Hi, intermediate hypothalamus; DHi, diffuse nucleus of the
1324 intermediate hypothalamus; Hc, caudal hypothalamus; Pit, pituitary; NL, neuropil layers (optic tectum); PL,
1325 periventricular cell layer (optic tectum); T, tegmentum; nMLF, nucleus of medial longitudinal fascicle; nIII,
1326 oculomotor nerve nucleus; TL, torus longitudinalis; TS, torus semicircularis; R1, rhombomere 1; nIV,
1327 trochlear nerve motor nucleus; IPN, interpeduncular nucleus; SR, superior raphe; CCe, corpus cerebelli; Va,
1328 valvula cerebelli; EG, eminentia granularis; LCa, lobus caudalis cerebelli; MON, medial octavolateralis
1329 nucleus; R2, rhombomere 2; nVd, dorsal motor nucleus of trigeminal nerve; R3, rhombomere 3; nVv, ventral
1330 motor nucleus of trigeminal nerve; IR, inferior raphe; R4, rhombomere 4; R5, rhombomere 5; MVN, medial
1331 vestibular nucleus; TVN, tangential vestibular nucleus; nVIIr, rostral facial nerve motor nucleus and
1332 octavolateralis efferent neurons; nVIr, rostral motor nucleus of abducens nerve; R6, rhombomere 6; nVIIc,
1333 caudal facial nerve motor nucleus and octavolateralis efferent neurons; nVIc, caudal motor nucleus of
1334 abducens nerve; R7, rhombomere 7; R8, rhombomere 8; nIX/X, glossopharyngeal/vagal nerve motor nucleus;
1335 VLo, vagal lobe; IO, inferior olive. See also Extended Data Figs. 5,6; Supplementary Table 3,4,5.
1336
1337 **Fig. 4 | Spatial organization and shared mode of LC-NE input architecture. a,** Rendering of all 374
1338 EM-reconstructed presynaptic neurons with identified somata that innervate LC-NE neuron #3. Based on their
1339 soma locations, which were empirically classified as sensory or motor-related, these presynaptic neurons were
1340 categorized into two types. Sensory-related (magenta), n_{neuron} = 159, $n_{synapse}$ = 182; Motor-related (blue), n_{neuron}
1341 = 215, $n_{synapse}$ = 236. The same color scheme is applied to all related panels below. In total, They form 418

synapses with LC-NE neuron #3, accounting for ~75% of its total dendritic inputs (n = 560). All synapses were traced; only those successfully traced back to their somata are shown. **b,** Regional distribution of presynaptic neurons with different modalities. Neuron counts are shown in parentheses. R1 and R2 ranked as the two predominant input sources, accounting for 20.86% and 10.16% of total inputs, respectively. **c,** 2D spatial distribution of dendritic inputome on LC-NE neuron #3. Each color-coded dot represents a single synaptic input site. In zebrafish, LC-NE neurons are pseudounipolar neurons, with both axonal and dendritic processes emerging from a primary branch. **d,e,** The relationship between the synaptic location's distance from the LC-NE neuron soma and the corresponding synaptic strength quantified by both PSD volume (panel **d**) and SV volume (panel **e**). Linear regression: Sensory-related, PSD volume versus path length, Y = -11,950 × X + 4,949,000; R^2 = 0.0637, P = 0.0006, $n_{sensory}$ = 182; Motor-related, PSD volume versus path length, Y = -21,720 × X + 5,682,000; R^2 = 0.1365, P < 0.0001, n_{motor} = 236; Sensory-related, SV volume versus path length, Y = -32,280 × X + 9,269,000; R^2 = 0.0686, P = 0.0004, $n_{sensory}$ = 182; Motor-related, SV volume versus path length, Y = -36,210 × X + 8,407,000; R^2 = 0.0797, P < 0.0001, n_{motor} = 236. Distribution of the probability density for the path length (top), PSD volume (top-right), and SV volume (bottom-right) is shown. $^{***}P$ < 0.001 (Mann Whitney U test). **f,** Schematic diagram of *in vivo* two-photon calcium imaging on LC-NE neurons' somata and dendrites, conducted in 6-dpf *Ki(dbh:GAL4-VP16);Tg(UAS:GCaMP6s);Tg(UAS:mCherry)* larvae. Simultaneous EMG recording was performed during imaging, with manual delivery of visual and auditory stimuli (left). The somatodendritic areas of LC-NE neurons in the population are shown, with the ventral direction indicated by a white arrow (right). **g,h,** Statistical analysis of auditory, visual, and motor-related responses of population LC-NE neurons' somata (panel **g**) and dendrites (panel **h**). Each dot represents the average peak response in individual larvae. $^{*}P$ < 0.05, $^{**}P$ < 0.01 (Paired t test). Error bars represent mean ± SEM. **i,** Rendering of all 72 EM-reconstructed intra-CPIs with identified somata that innervate LC-NE neuron #3. Sensory-related (magenta), n_{neuron} = 30, $n_{synapse}$ = 39; Motor-related (blue), n_{neuron} = 39, $n_{synapse}$ = 49. **j,** Regional distribution of intra-CPIs with different modalities. Neuron counts are shown in parentheses. **k,** Proportion of intra-CPI-to-LC synapses relative to all synaptic inputs received by LC-NE neuron #3. **l,** Proportion of intra-CPIs with varying targeting numbers. **m,** Rendering of all intra-CPIs targeting LC-NE neuron #3 with the targeting numbers color-coded. **n,** Rendering of all 26 EM-reconstructed inter-CPIs with identified somata that innervate LC-NE neuron #3. Sensory-related (magenta), n_{neuron} = 12, $n_{synapse}$ = 17; Motor-related (blue), n_{neuron} = 14, $n_{synapse}$ = 15. **o,** Regional distribution of inter-CPIs with different modalities. Neuron counts are shown in parentheses. **p,** Proportion of inter-CPI-to-LC synapses relative to all synaptic inputs received by LC-NE neuron #3. **q,** Different shared innervation combinations. **r,** Rendering of all inter-CPIs targeting LC-NE neuron #3 with the combinations color-coded. Additionally, two inter-CPIs that innervate three monoaminergic systems simultaneously are shown. However, these two neurons target other LC-NE neurons, rather than #3. **s,** Schematic diagram of *in vivo* confocal imaging on multiple monoaminergic systems conducted in 6-dpf *Ki(th:GAL4-VP16);Ki(tph2:GAL4FF,cmlc2:EGFP);Tg(UAS:GCaMP6s)* larvae. **t,** Heatmap depicting spontaneous calcium activities in three monoaminergic systems, with z-scored relative fluorescence changes color-coded. White arrowheads indicate synchronous activities between LC-NE and PT-DA neurons. **u,** Schematic diagram of dendritic input architecture in the LC-NE system. Scale bars, 10 μm

(panel **f**), 50 μm (panel **m,r**). C, caudal; Ri, right; V, ventral; Po, preoptic region; OTAOS, optic tract and accessory optic system; Pr, pretectum; Ha, habenula; DT, dorsal thalamus; VT, ventral thalamus; PT, posterior tuberculum; M2, migrated posterior tubercular region; Hr, rostral hypothalamus; Hi, intermediate hypothalamus; Hc, caudal hypothalamus; PL, periventricular cell layer (optic tectum); T, tegmentum; nMLF, nucleus of medial longitudinal fascicle; nIII, oculomotor nerve nucleus; TS, torus semicircularis; R1, rhombomere 1; nIV, trochlear nerve motor nucleus; IPN, interpeduncular nucleus; SR, superior raphe; CCe, corpus cerebelli; EG, eminentia granularis; MON, medial octavolateralis nucleus; R2, rhombomere 2; nVd, dorsal motor nucleus of trigeminal nerve; R3, rhombomere 3; IR, inferior raphe; R4, rhombomere 4; R5, rhombomere 5; nVIIr, rostral facial nerve motor nucleus and octavolateralis efferent neurons; R6, rhombomere 6; R7, rhombomere 7. See also Extended Data Figs. 7,8.

1392 **Extended Data Figure Legends**

1393 **Extended Data Fig. 1 | Multiplexed APEX2-labeled transgenic fish line. a,** Summary of nuclei and
1394 corresponding neuronal types exhibiting distinct APEX2-labeling patterns in the quadruple transgenic fish line.
1395 Brain region annotation was achieved through correlative light and electron microscopy (CLEM), followed by
1396 manual validation. **b,** Validation of APEX2-labeled neurons' specificity in the quadruple transgenic fish line at
1397 6 dpf through immunohistochemical staining and comparison with published stable fish lines. Top panels,
1398 signals from red fluorescent proteins conjugated with APEX2; Middle panels, immunofluorescence signals or
1399 signals from green fluorescent proteins in stable fish lines; Bottom panels, merged images. For validating
1400 noradrenergic (e.g., LC-NE) and dopaminergic neurons (e.g., PT-DA),
1401 *Gt(vmat2:GAL4FF);Tg(dbh:GAL4FF;UAS:cytosol-APEX2-TagRFP)* larvae were stained using tyrosine
1402 hydroxylase antibody. For validating Hcrt neurons, *Tg(hcrt:APEX2-TagRFP-NLS)* larvae were stained using
1403 hypocretin antibody. *Ki(tph2:EGFP)* and *Tg(glyt2:GFP)* larvae were used to validate serotonergic and
1404 glycinergic neurons, respectively. **c,** The fluorescent images of the 6-dpf multiplexed APEX2-labeled larva
1405 (Fish-X) used in this study. Z-projected whole-brain (left panel) and expanded (right panels) fluorescent
1406 images are shown. Three expanded images display the cytoplasmic, nuclear, and mitochondrial-localized
1407 APEX2 signals, indicated by white arrows or dashed white contours, in OB-DA, Hcrt, and Gly neurons,
1408 respectively. **d,** Quantification of APEX2-labeled neurons and their ratio to the theoretical population size
1409 (labeling efficiency). Except for Gly neurons, the remaining APEX2-labeled neurons were manually counted.
1410 Gly neurons were automatically identified based on somatic presence of ≥4 APEX2-labeled mitochondria.
1411 Theoretical neuron counts for each type were derived from the average of manual counts, calculated from
1412 fluorescent images of stable fish lines, across three individuals. Scale bars, 10 μm (panels **b,c**), 50 μm (panel
1413 **c**). Ro, rostral; C, caudal; Ri, right; L, left; LC, locus coeruleus; MO, medulla oblongata; OB, olfactory bulb;
1414 PT, posterior tuberculum; Hc, caudal hypothalamus; SR, superior raphe; IR, inferior raphe; Pr, pretectum; NE,
1415 noradrenergic; DA, dopaminergic; 5HT, serotonergic; Hcrt, hypocretinergic; Gly, glycinergic.

1416

1417 **Extended Data Fig. 2 | The detailed workflow for whole-brain ssEM of larval zebrafish. a,** The workflow
1418 includes live confocal fluorescence imaging, DAB staining, rOTO staining, dehydration, resinification, X-ray
1419 micro-tomography, ATUM-SEM, image stitching, 3D registration, 3D reconstruction, CLEM combined with
1420 the Zebrafish Mesoscopic Atlas, proofreading, and 3D visualization. See Methods for details. **b,** Rendering of
1421 a randomly selected ~2.7% (4,731) of all automatically reconstructed cells within the brain. **c,** Magnified
1422 rendering of 1,533 automatically reconstructed cells in bilateral optic tectum. The inset displays the optic
1423 tectum, which is marked in yellow. Scale bars, 50 μm (panel **c**), 100 μm (panel **b**). C, caudal; L, left; V, ventral.
1424 See also Supplementary Table 1.

1425

1426 **Extended Data Fig. 3 | Brain-wide cell type diversity. a,** Nucleus density distribution across 52 major brain
1427 regions in the brain and 7 regions in the retina. **b,** Brain regions compatible with the ssEM dataset were
1428 established through CLEM, followed by manual validation. **c,d,** UMAP visualization of nucleus clustering of
1429 176,789 cells (panel **c**) and only cells with annotated cell types (panel **d**) in the brain using combined
1430 deep-learned and traditional features. 21 cells were excluded from clustering due to incomplete nuclear

morphology resulting from their localization at dataset boundaries. All nuclei underwent sequential automated segmentation followed by manual verification, achieving optimal 3D morphological reconstruction. In total, 1,169 cells were manually annotated with cell types (n_{EC} = 383, purple circles; n_{PC} = 84, green circles; n_{RBC} = 44, orange or red circles; $n_{LC\text{-}NE}$ = 12, solid orange circles; $n_{MO\text{-}NE}$ = 54, solid orange triangles; $n_{OB\text{-}DA}$ = 38, solid green squares; $n_{Hc\text{-}DA}$ = 45, solid green triangles; $n_{PT\text{-}DA}$ = 22, solid green circles; $n_{Pr\text{-}5HT}$ = 9, solid blue triangles; $n_{SR/IR\text{-}5HT}$ = 117, solid blue circles; n_{Hcrt} = 12, solid magenta circles; n_{Gly} = 349, solid light blue circles). Besides, 70,114 cells, whose automatically reconstructed supervoxels possess at least one synapse, were presumed as neurons. The remaining were presumed to be glial cells, or neurons embedded in somata regions which processes were not well automatically reconstructed. **e,** Representative EM images (left panels) and renderings (right panels) of nuclei from varying cell types. Nuclei are indicated by white asterisks. **f,** Comparisons of nuclear-to-cytoplasmic volume ratio and somatic mitochondrial density between multiple APEX2-labeled neuronal types, which counts are shown in parentheses. For each APEX2-labeled neuron, features from the soma and nucleus of 10 adjacent cells were extracted for comparison. **g,** UMAP visualization of clustering of all cells in panel **f** using combined deep-learned and traditional features of their nuclei and somata. Scale bars, 3 μm (panel **e**), 50 μm (panel **b**). C, caudal; L, left. OB, olfactory bulb; P, pallium; S, subpallium; Po, preoptic region; OTAOS, optic tract and accessory optic system; Pr, pretectum; E, epiphysis; Ha, habenula; DT, dorsal thalamus; VT, ventral thalamus; PT, posterior tuberculum; M2, migrated posterior tubercular region; Hr, rostral hypothalamus; Hi, intermediate hypothalamus; DHi, diffuse nucleus of the intermediate hypothalamus; Hc, caudal hypothalamus; Pit, pituitary; NL, neuropil layers (optic tectum); PL, periventricular cell layer (optic tectum); T, tegmentum; nMLF, nucleus of medial longitudinal fascicle; nIII, oculomotor nerve nucleus; TL, torus longitudinalis; TS, torus semicircularis; R1, rhombomere 1; nIV, trochlear nerve motor nucleus; IPN, interpeduncular nucleus; SR, superior raphe; CCe, corpus cerebelli; Va, valvula cerebelli; EG, eminentia granularis; LCa, lobus caudalis cerebelli; MON, medial octavolateralis nucleus; R2, rhombomere 2; nVd, dorsal motor nucleus of trigeminal nerve; R3, rhombomere 3; nVv, ventral motor nucleus of trigeminal nerve; IR, inferior raphe; R4, rhombomere 4; R5, rhombomere 5; MVN, medial vestibular nucleus; TVN, tangential vestibular nucleus; nVIIr, rostral facial nerve motor nucleus and octavolateralis efferent neurons; nVIr, rostral motor nucleus of abducens nerve; R6, rhombomere 6; nVIIc, caudal facial nerve motor nucleus and octavolateralis efferent neurons; nVIc, caudal motor nucleus of abducens nerve; R7, rhombomere 7; R8, rhombomere 8; nIX/X, glossopharyngeal/vagal nerve motor nucleus; VLo, vagal lobe; IO, inferior olive; ONL, outer nuclear layer; OPL, Outer plexiform layer; INL, inner nuclear layer; IPL, inner plexiform layer; RGCL, retinal ganglion cell layer; CMZ, ciliary marginal zone; ON, optic nerve; EC, endothelial cells; PC, pericytes; RBC, red blood cells. See also Supplementary Table 1,2

Extended Data Fig. 4 | Identification of E/I synapses using mitochondrial-localized APEX2. a, Schematic diagram of labeling glutamatergic and GABAergic neurons using mitochondrial-localized APEX2. The plasmid *5×UAS-2×Cox8a-APEX2-TagRFP* was used to specifically label mitochondria in glutamatergic or GABAergic neurons under the control of *vglut2a* or *gad1b* promoters, respectively. **b,c,** Representative EM images of APEX2-labeld mitochondria in glutamatergic (panel **b**) and GABAergic (panel **c**) neurons. APEX2-labeled mitochondria were indicated by dashed red contours and PSDs were indicated by yellow

arrows. **d,** Comparisons of ultrastructural features between glutamatergic (n = 101) and GABAergic (n = 116) synapses, where mitochondria were labeled using APEX2. Scale bars, 200 nm (panels **b,c**).

Extended Data Fig. 5 | Region-specific distributions of PSDs, SVs, and mitochondria. a,b,c, Density distribution of PSDs (panel **a**), SVs (panel **b**), and mitochondria (panel **c**) across 52 major brain regions in the whole brain. PSDs, SVs, and mitochondria were automatically identified. OB, olfactory bulb; P, pallium; S, subpallium; Po, preoptic region; OTAOS, optic tract and accessory optic system; Pr, pretectum; E, epiphysis; Ha, habenula; DT, dorsal thalamus; VT, ventral thalamus; PT, posterior tuberculum; M2, migrated posterior tubercular region; Hr, rostral hypothalamus; Hi, intermediate hypothalamus; DHi, diffuse nucleus of the intermediate hypothalamus; Hc, caudal hypothalamus; Pit, pituitary; NL, neuropil layers (optic tectum); PL, periventricular cell layer (optic tectum); T, tegmentum; nMLF, nucleus of medial longitudinal fascicle; nIII, oculomotor nerve nucleus; TL, torus longitudinalis; TS, torus semicircularis; R1, rhombomere 1; nIV, trochlear nerve motor nucleus; IPN, interpeduncular nucleus; SR, superior raphe; CCe, corpus cerebelli; Va, valvula cerebelli; EG, eminentia granularis; LCa, lobus caudalis cerebelli; MON, medial octavolateralis nucleus; R2, rhombomere 2; nVd, dorsal motor nucleus of trigeminal nerve; R3, rhombomere 3; nVv, ventral motor nucleus of trigeminal nerve; IR, inferior raphe; R4, rhombomere 4; R5, rhombomere 5; MVN, medial vestibular nucleus; TVN, tangential vestibular nucleus; nVIIr, rostral facial nerve motor nucleus and octavolateralis efferent neurons; nVIr, rostral motor nucleus of abducens nerve; R6, rhombomere 6; nVIIc, caudal facial nerve motor nucleus and octavolateralis efferent neurons; nVIc, caudal motor nucleus of abducens nerve; R7, rhombomere 7; R8, rhombomere 8; nIX/X, glossopharyngeal/vagal nerve motor nucleus; VLo, vagal lobe; IO, inferior olive. See also Supplementary Table 3,4,5.

Extended Data Fig. 6 | Scale-distinct innervation exerted by various NM neurons. a,b,c,d,e,f,g,h, Representative examples of single-cell morphologies with varying NM types, including LC-NE (panel **a**), MO-NE (panel **b**), SR-5HT (panel **c**), Pr-5HT (panel **d**), PT-DA (panel **e**), OB-DA (panel **f**), Hc-DA (panel **g**), and Hcrt (panel **h**) neurons, from the Zebrafish Mesoscopic Atlas. The predominantly innervated neuropil is highlighted in light blue, which is shown in parentheses below. NE, noradrenergic; DA, dopaminergic; 5HT, serotonergic; Hcrt, hypocretinergic; Gly, glycinergic; LC, locus coeruleus; MO, medulla oblongata; SR, Superior raphe; Pr, pretectum; OB, olfactory bulb; S, subpallium; OTAOS, optic tract and accessory optic system; M2, migrated posterior tubercular region; Hr, rostral hypothalamus; Hi, intermediate hypothalamus; Hc, caudal hypothalamus; NL, neuropil layers (optic tectum); T, tegmentum; MON, medial octavolateralis nucleus; R2, rhombomere 2; R3, rhombomere 3; R4, rhombomere 4; R6, rhombomere 6.

Extended Data Fig. 7 | Localized unitary inputs to OB-DA and Pr-5HT neurons. a, Rendering of a single EM-reconstructed OB-DA neuron (green) and its presynaptic neurons (Gray, n = 9) with identified somata. All 20 synapses were traced; only those successfully traced back to their somata are shown. **b,c,** Renderings of a single EM-reconstructed Pr-5HT neuron (blue) and its presynaptic neurons' axons (Gray, n = 24) in dorsal (panel **b**) and front (panel **c**) views, respectively. All synapses (n = 29) were traced; however, no synapse was traced back to its soma.The inset displays the reconstructed regions, which are marked in yellow. Dashed

magenta contours indicate AF9. Scale bars, 50 μm (panels **a,b,c**). C, caudal; L, left; V, ventral; DA, dopaminergic; 5HT, serotonergic; OB, olfactory bulb; Pr, pretectum; AF9, arborization field 9.

Extended Data Fig. 8 | Heterogeneity in dendritic inputs among individual LC-NE neurons. a,b,c,d, Renderings of EM-reconstructed presynaptic neurons with identified somata that innervate LC-NE neuron #1 (panel **a**), #2 (panel **b**), #3 (panel **c**), and #4 (panel **d**), respectively. The number of presynaptic neurons traced back to their somata (n_{neuron}), the corresponding count of synapses formed between these neurons and the target LC-NE neuron ($n_{synapse}$), and the ratio of soma-traced synapses to total synapses per LC-NE neuron ($Coverage_{synapse}$) are shown below. Notably, two Hcrt neurons (magenta) with nuclear-localized APEX2 specifically targeted LC-NE neuron #4, rather than other LC-NE neurons. Scale bars, 50 μm (panels **a,b,c,d**). Ro, rostral; V, ventral.

1521 **Supplementary Information**

1522 **Supplementary Table 1 |** Standardized nomenclature of brain regions
1523 **Supplementary Table 2 |** Nuclei counts and density across brain regions
1524 **Supplementary Table 3 |** PSDs counts and density across brain regions
1525 **Supplementary Table 4 |** SVs counts and density across brain regions
1526 **Supplementary Table 5 |** Mitochondria counts and density across brain regions
1527

1528 **Supplementary Table 1 | Standardized nomenclature of brain regions**

Region_id	Name	Abbr.	Volume (μm^3)
1	Olfactory bulb	OB	552,907.80
2	Pallium	P	1,176,906.63
3	Subpallium	S	954,796.37
4	Preoptic region	Po	759,356.45
5	Optic tract and accessory optic system	OTAOS	986,748.95
6	Pretectum	Pr	669,170.64
7	Epiphysis (Pineal gland)	E	110,533.43
8	Habenula	Ha	289,854.83
9	Dorsal thalamus	DT	286,673.99
10	Ventral thalamus	VT	336,431.48
11	Posterior tuberculum	PT	377,980.15
12	Migrated posterior tubercular region	M2	658,202.84
13	Rostral hypothalamus	Hr	1,204,135.20
14	Intermediate hypothalamus	Hi	1,874,093.02
15	Diffuse nucleus of the intermediate hypothalamus	DHi	250,549.79
16	Caudal hypothalamus	Hc	176,238.95
17	Pituitary	Pit	83,580.57
18	Neuropil layer (optic tectum)	NL	2,939,375.09
19	Periventricular cell layer (optic tectum)	PL	3,760,502.17
20	Tegmentum	T	536,864.29
21	Nucleus of medial longitudinal fascicle	nMLF	30,611.07
22	Oculomotor nerve nucleus	nIII	77,251.04
23	Torus longitudinalis	TL	115,042.14
24	Torus semicircularis	TS	1,105,957.84
25	Rhombomere 1	R1	1,829,045.90
26	Trochlear nerve motor nucleus	nIV	50,476.46
27	Interpeduncular nucleus	IPN	196,849.62
28	Superior Raphe	SR	122,206.58
29	Corpus cerebelli	CCe	1,345,996.74
30	Valvula cerebelli	Va	282,478.01
31	Eminentia granularis	EG	270,844.81
32	Lobus caudalis cerebelli	LCa	32,741.70
33	Medial octavolateralis nucleus	MON	274,799.18
34	Rhombomere 2	R2	1,039,406.70
35	Dorsal motor nucleus of trigeminal nerve	nVd	36,112.51
36	Rhombomere 3	R3	897,971.87
37	Ventral motor nucleus of trigeminal nerve	nVv	16,845.30
38	Inferior raphe	IR	32,603.36
39	Rhombomere 4	R4	891,197.12
40	Rhombomere 5	R5	1,038,459.75
41	Medial vestibular nucleus	MVN	35,611.76
42	Tangential vestibular nucleus	TVN	30,629.58

43	Rostral facial nerve motor nucleus and octavolateralis efferent neurons	nVIIr/OLer	68,704.18
44	Rostral motor nucleus of abducens nerve	nVIr	6,896.53
45	Rhombomere 6	R6	1,048,429.95
46	Caudal facial nerve motor nucleus and octavolateralis efferent neurons	nVIIc/OLec	22,639.00
47	Caudal motor nucleus of abducens nerve	nVIc	14,460.40
48	Rhombomere 7	R7	930,447.61
49	Rhombomere 8	R8	1,964,286.62
50	Glossopharyngeal/Vagal nerve motor nucleus	nIX/X	188,459.61
51	Vagal lobe	VLo	15,311.87
52	Inferior olive	IO	37,314.70
53	Outer nuclear layer	ONL	1,935,701.58
54	Outer plexiform layer	OPL	218,800.10
55	Inner nuclear layer	INL	1,811,315.73
56	Inner plexiform layer	IPL	642,129.04
57	Retinal ganglion cell layer	RGCL	447,158.97
58	Ciliary marginal zone	CMZ	88,195.60
59	Optic nerve	ON	8,981.38

1530 **Supplementary Table 2 | Nuclei counts and density across brain regions**

Region_id	Name (abbr.)	Count	Density (per 10^3 μm^3)
1	OB	2,937	5.31
2	P	6,056	5.15
3	S	5,380	5.63
4	Po	4,733	6.23
5	OTAOS	2,380	2.41
6	Pr	5,021	7.50
7	E	461	4.17
8	Ha	2,020	6.97
9	DT	2,347	8.19
10	VT	2,875	8.55
11	PT	2,541	6.72
12	M2	1,738	2.64
13	Hr	4,398	3.65
14	Hi	6,934	3.70
15	DHi	1,589	6.34
16	Hc	1,399	7.94
17	Pit	616	7.37
18	NL	1,489	0.51
19	PL	39,919	10.62
20	T	3,098	5.77
21	nMLF	224	7.32
22	nIII	616	7.97
23	TL	864	7.51
24	TS	6,646	6.01
25	R1	9,401	5.14
26	nIV	503	9.97
27	IPN	524	2.66
28	SR	887	7.26
29	CCe	9,287	6.90
30	Va	2,184	7.73
31	EG	2,233	8.24
32	LCa	314	9.59
33	MON	467	1.70
34	R2	5,307	5.11
35	nVd	241	6.67
36	R3	4,313	4.80
37	nVv	65	3.86
38	IR	152	4.66
39	R4	3,822	4.29
40	R5	5,856	5.64
41	MVN	155	4.35
42	TVN	70	2.29

43	nVIIr/OLer	488	7.10
44	nVIr	25	3.63
45	R6	5,376	5.13
46	nVIIc/OLec	130	5.74
47	nVIc	36	2.49
48	R7	5,031	5.41
49	R8	11,784	6.00
50	nIX/X	1,430	7.59
51	VLo	96	6.27
52	IO	267	7.16
53	ONL	23,576	12.18
54	OPL	1,122	5.13
55	INL	38,063	21.01
56	IPL	89	0.14
57	RGCL	6,988	15.63
58	CMZ	1,051	11.92
59	ON	21	2.34

1532 **Supplementary Table 3 | PSDs counts and density across brain regions**

Region_id	Name (abbr.)	Count	Density (per 10^3 μm^3)
1	OB	168,961	305.59
2	P	619,202	526.13
3	S	570,921	597.95
4	Po	397,593	523.59
5	OTAOS	969,580	982.60
6	Pr	185,228	276.80
7	E	5,371	48.59
8	Ha	74,603	257.38
9	DT	51,797	180.68
10	VT	59,776	177.68
11	PT	194,962	515.80
12	M2	890,300	1,352.62
13	Hr	1,248,748	1,037.05
14	Hi	2,269,327	1,210.89
15	DHi	47,967	191.45
16	Hc	29,554	167.69
17	Pit	6,949	83.14
18	NL	6,274,593	2,134.67
19	PL	143,460	38.15
20	T	488,299	909.54
21	nMLF	4,158	135.83
22	nIII	20,325	263.10
23	TL	10,079	87.61
24	TS	997,075	901.55
25	R1	1,817,808	993.86
26	nIV	3,156	62.52
27	IPN	235,891	1,198.33
28	SR	31,382	256.79
29	CCe	543,830	404.04
30	Va	55,456	196.32
31	EG	94,508	348.94
32	LCa	256	7.82
33	MON	387,594	1,410.46
34	R2	1,024,545	985.70
35	nVd	6,723	186.17
36	R3	768,601	855.93
37	nVv	17,612	1,045.51
38	IR	11,246	344.93
39	R4	746,597	837.75
40	R5	660,500	636.04
41	MVN	15,087	423.65
42	TVN	31,957	1,043.34

43	nVIIr/OLer	10,745	156.40
44	nVIr	8,262	1,197.99
45	R6	750,372	715.71
46	nVIIc/OLec	1,141	50.40
47	nVIc	18,099	1,251.63
48	R7	864,232	928.83
49	R8	1,309,422	666.61
50	nIX/X	82,721	438.93
51	VLo	3,171	207.09
52	IO	17,618	472.15

1533

1534 **Supplementary Table 4 | SVs counts and density across brain regions**

Region_id	Name (abbr.)	Count	Density (per 10^3 μm^3)
1	OB	157,880	285.54
2	P	440,095	373.94
3	S	418,483	438.30
4	Po	274,409	361.37
5	OTAOS	567,745	575.37
6	Pr	107,340	160.41
7	E	6,561	59.36
8	Ha	38,386	132.43
9	DT	28,278	98.64
10	VT	34,647	102.98
11	PT	111,957	296.20
12	M2	578,311	878.62
13	Hr	756,460	628.22
14	Hi	1,493,329	796.83
15	DHi	28,689	114.50
16	Hc	20,016	113.57
17	Pit	11,688	139.84
18	NL	3,864,426	1,314.71
19	PL	81,328	21.63
20	T	325,770	606.80
21	nMLF	1,988	64.94
22	nIII	11,687	151.29
23	TL	6,317	54.91
24	TS	584,917	528.88
25	R1	1,091,715	596.88
26	nIV	1,351	26.76
27	IPN	223,406	1,134.91
28	SR	18,389	150.47
29	CCe	412,867	306.74
30	Va	51,639	182.81
31	EG	45,662	168.59
32	LCa	137	4.18
33	MON	179,624	653.66
34	R2	587,247	564.98
35	nVd	4,383	121.37
36	R3	439,578	489.52
37	nVv	9,836	583.90
38	IR	8,031	246.32
39	R4	447,452	502.08
40	R5	396,779	382.08
41	MVN	9,154	257.05
42	TVN	17,689	577.51

43	nVIIr/OLer	7,489	109.00
44	nVIr	5,165	748.93
45	R6	457,744	436.60
46	nVIIc/OLec	814	35.96
47	nVIc	11,255	778.33
48	R7	516,297	554.89
49	R8	809,742	412.23
50	nIX/X	50,822	269.67
51	VLo	2,377	155.24
52	IO	12,457	333.84

1536 **Supplementary Table 5 | Mitochondria counts and density across brain regions**

Region_id	Name (abbr.)	Count	Density (per 10^3 μm^3)
1	OB	146,644	265.22
2	P	365,682	310.71
3	S	364,324	381.57
4	Po	247,663	326.15
5	OTAOS	535,443	542.63
6	Pr	133,626	199.69
7	E	11,706	105.90
8	Ha	58,557	202.02
9	DT	45,091	157.29
10	VT	47,103	140.01
11	PT	107,722	284.99
12	M2	411,387	625.02
13	Hr	617,761	513.03
14	Hi	1,115,733	595.35
15	DHi	30,243	120.71
16	Hc	34,030	193.09
17	Pit	17,205	205.85
18	NL	2,582,241	878.50
19	PL	265,164	70.51
20	T	303,911	566.09
21	nMLF	3,942	128.78
22	nIII	18,408	238.29
23	TL	15,109	131.33
24	TS	509,154	460.37
25	R1	905,849	495.26
26	nIV	4,828	95.65
27	IPN	217,883	1,106.85
28	SR	27,805	227.52
29	CCe	399,534	296.83
30	Va	65,467	231.76
31	EG	73,700	272.11
32	LCa	1,190	36.35
33	MON	251,781	916.24
34	R2	490,509	471.91
35	nVd	6,031	167.01
36	R3	402,701	448.46
37	nVv	6,147	364.91
38	IR	13,723	420.91
39	R4	427,100	479.24
40	R5	413,002	397.71
41	MVN	12,173	341.83
42	TVN	25,790	842.00

43	nVIIr/OLer	14,259	207.54
44	nVIr	4,869	706.01
45	R6	497,382	474.41
46	nVIIc/OLec	5,806	256.46
47	nVIc	12,623	872.94
48	R7	487,363	523.79
49	R8	866,776	441.27
50	nIX/X	54,772	290.63
51	VLo	3,139	205.00
52	IO	15,150	406.01

1537

1538 **Figures**

1539 **Fig. 1**

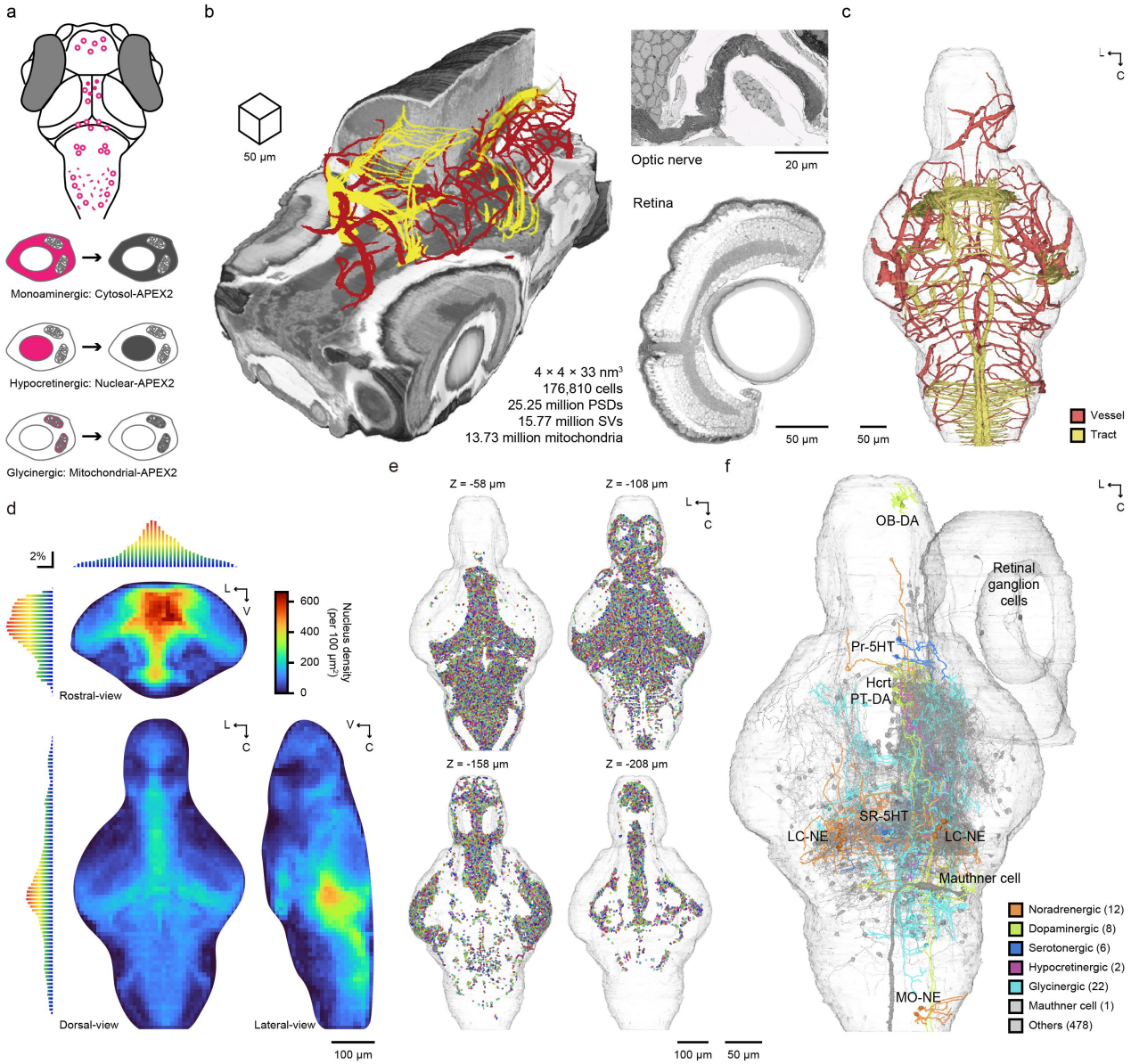

1540

1541

Fig. 2

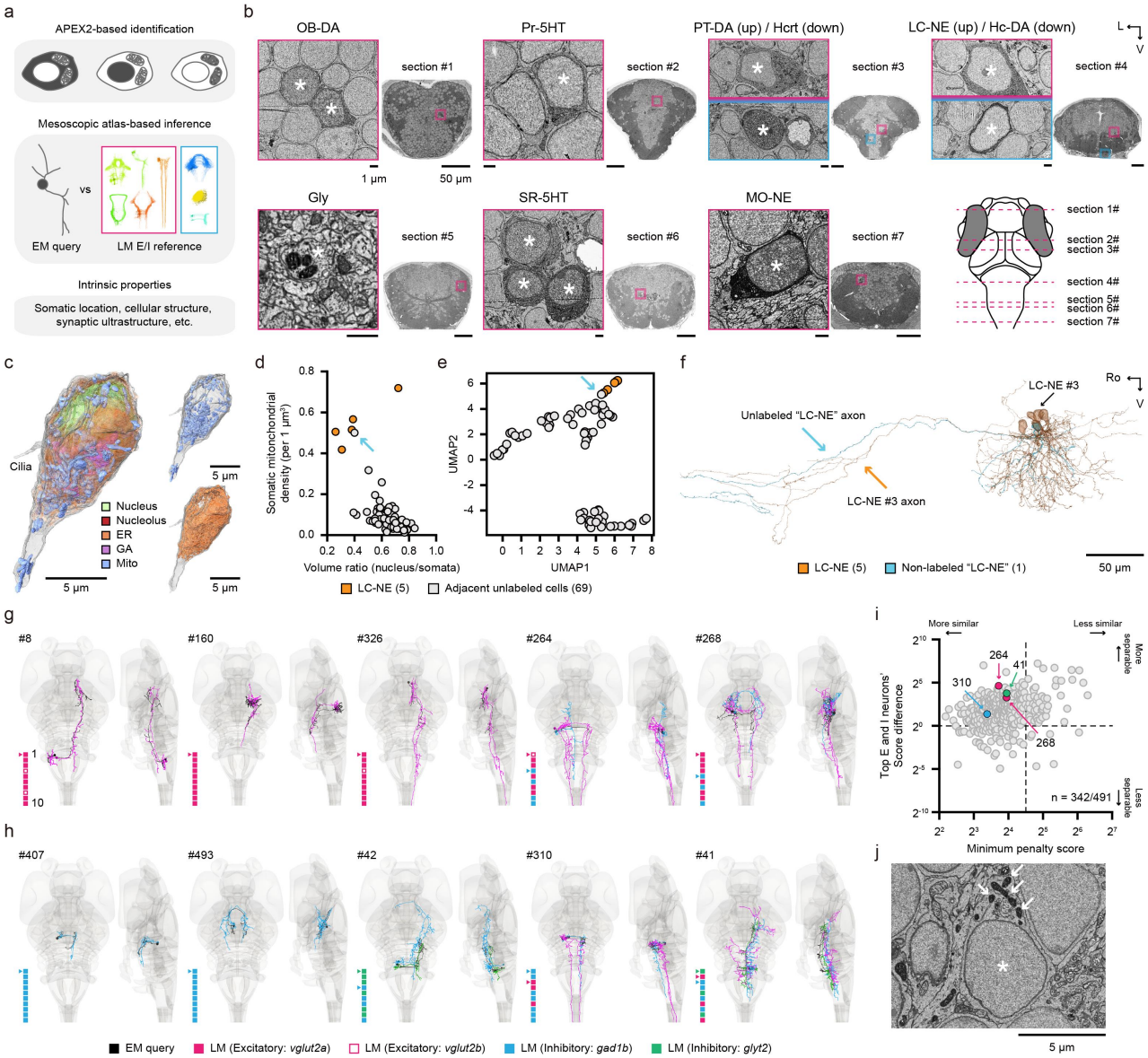
a
APEX2-based identification
Mesoscopic atlas-based inference
vs
EM query
LM E/I reference
Intrinsic properties
Somatic location, cellular structure, synaptic ultrastructure, etc.
b
OB-DA
Pr-5HT
PT-DA (up) / Hcrt (down)
LC-NE (up) / Hc-DA (down)
section #1
section #2
section #3
section #4
1 µm
50 µm
Gly
SR-5HT
MO-NE
section #5
section #6
section #7
section 1#
section 2#
section 3#
section 4#
section 5#
section 6#
section 7#
c
Cilia
Nucleus
Nucleolus
ER
GA
Mito
5 µm
d
Somatic mitonchondrial density (per 1 µm³)
Volume ratio (nucleus/somata)
e
UMAP2
UMAP1
LC-NE (5)
Adjacent unlabeled cells (69)
f
Unlabeled "LC-NE" axon
LC-NE #3
LC-NE #3 axon
Ro
V
LC-NE (5)
Non-labeled "LC-NE" (1)
50 µm
g
#8
#160
#326
#264
#268
h
#407
#493
#42
#310
#41
EM query
LM (Excitatory: vglut2a)
LM (Excitatory: vglut2b)
LM (Inhibitory: gad1b)
LM (Inhibitory: glyt2)
i
More similar
Less similar
More separable
Less separable
Top E and I neurons' Score difference
Minimum penalty score
n = 342/491
j
5 µm

Fig. 3

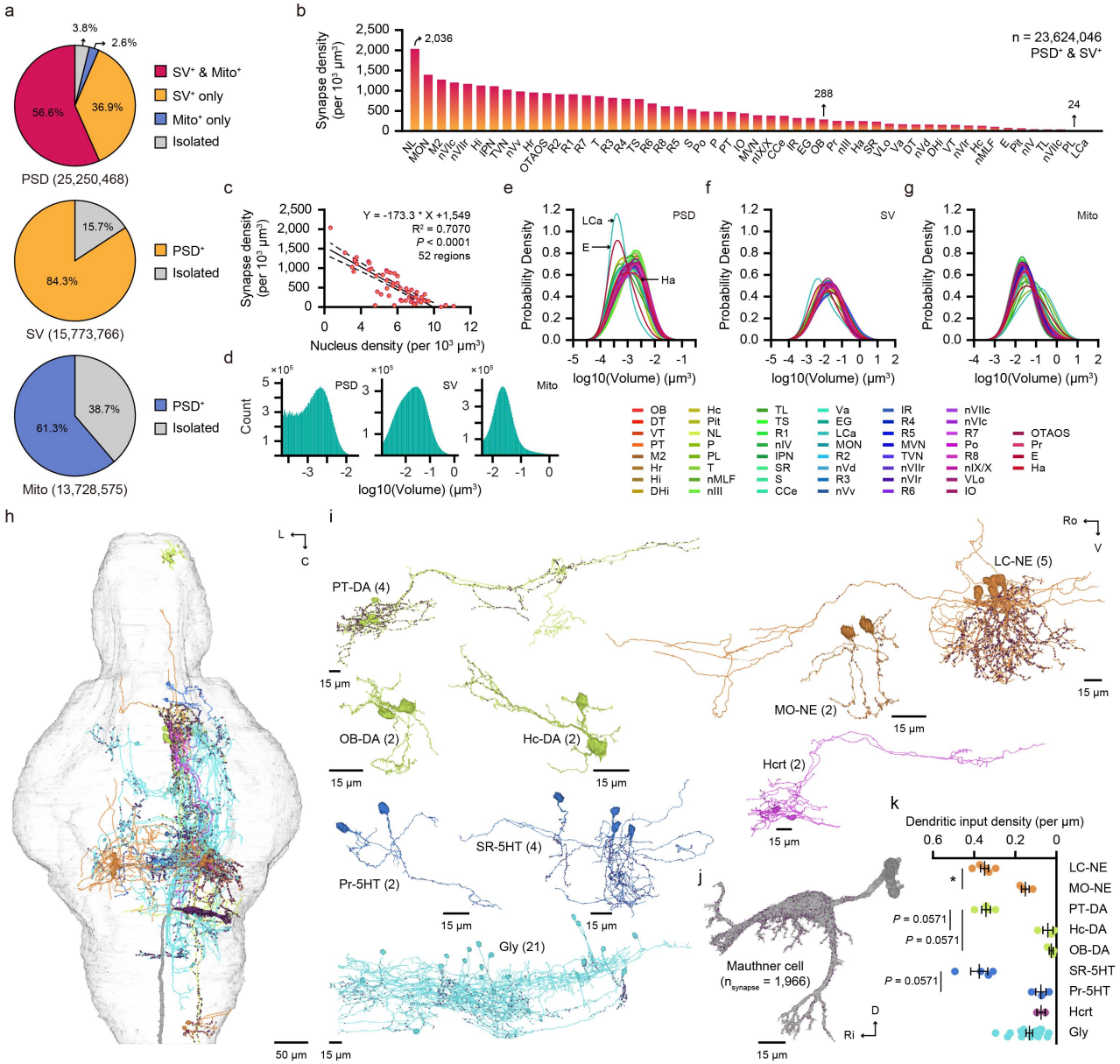
a
3.8%
2.6%
56.6%
36.9%
SV+ & Mito+
SV+ only
Mito+ only
Isolated
PSD (25,250,468)
15.7%
84.3%
PSD+
Isolated
SV (15,773,766)
38.7%
61.3%
PSD+
Isolated
Mito (13,728,575)
b
Synapse density (per 10³ µm³)
2,036
288
24
n = 23,624,046
PSD+ & SV+
NL MON M2 nVIc nVIIr Hi IPN TVN nVv Hr OTAOS R2 R1 R7 T R3 R4 Ts R6 R8 R5 S Po P PT IO MVN nIX/X CCe IR EG OB Pr nIII Ha SR VLo Va DT nVd DHi VT nVIr He nMLF E Pit nIV TL nVIIc PL LCa
c
Y = -173.3 * X +1,549
R² = 0.7070
P < 0.0001
52 regions
Synapse density (per 10³ µm³)
Nucleus density (per 10³ µm³)
d
PSD
SV
Mito
Count
log10(Volume) (µm³)
e
PSD
LCa
E
Ha
Probability Density
log10(Volume) (µm³)
f
SV
Probability Density
log10(Volume) (µm³)
g
Mito
Probability Density
log10(Volume) (µm³)
OB DT VT PT M2 Hr Hi DHi
Hc Pit NL P PL T nMLF nIII
TL TS R1 nIV IPN SR S CCe
Va EG LCa MON R2 nVd R3 nVv
IR R4 R5 MVN TVN nVIIr nVIr R6
nVIIc nVIc R7 Po R8 nIX/X VLo IO
OTAOS Pr E Ha
h
L
c
i
PT-DA (4)
OB-DA (2)
Hc-DA (2)
Pr-5HT (2)
SR-5HT (4)
Gly (21)
15 µm
50 µm
Ro
V
LC-NE (5)
MO-NE (2)
Hcrt (2)
j
Mauthner cell
(n synapse = 1,966)
D
Ri
k
Dendritic input density (per µm)
LC-NE
MO-NE
PT-DA
Hc-DA
OB-DA
SR-5HT
Pr-5HT
Hcrt
Gly
P = 0.0571
P = 0.0571
P = 0.0571

Fig. 4

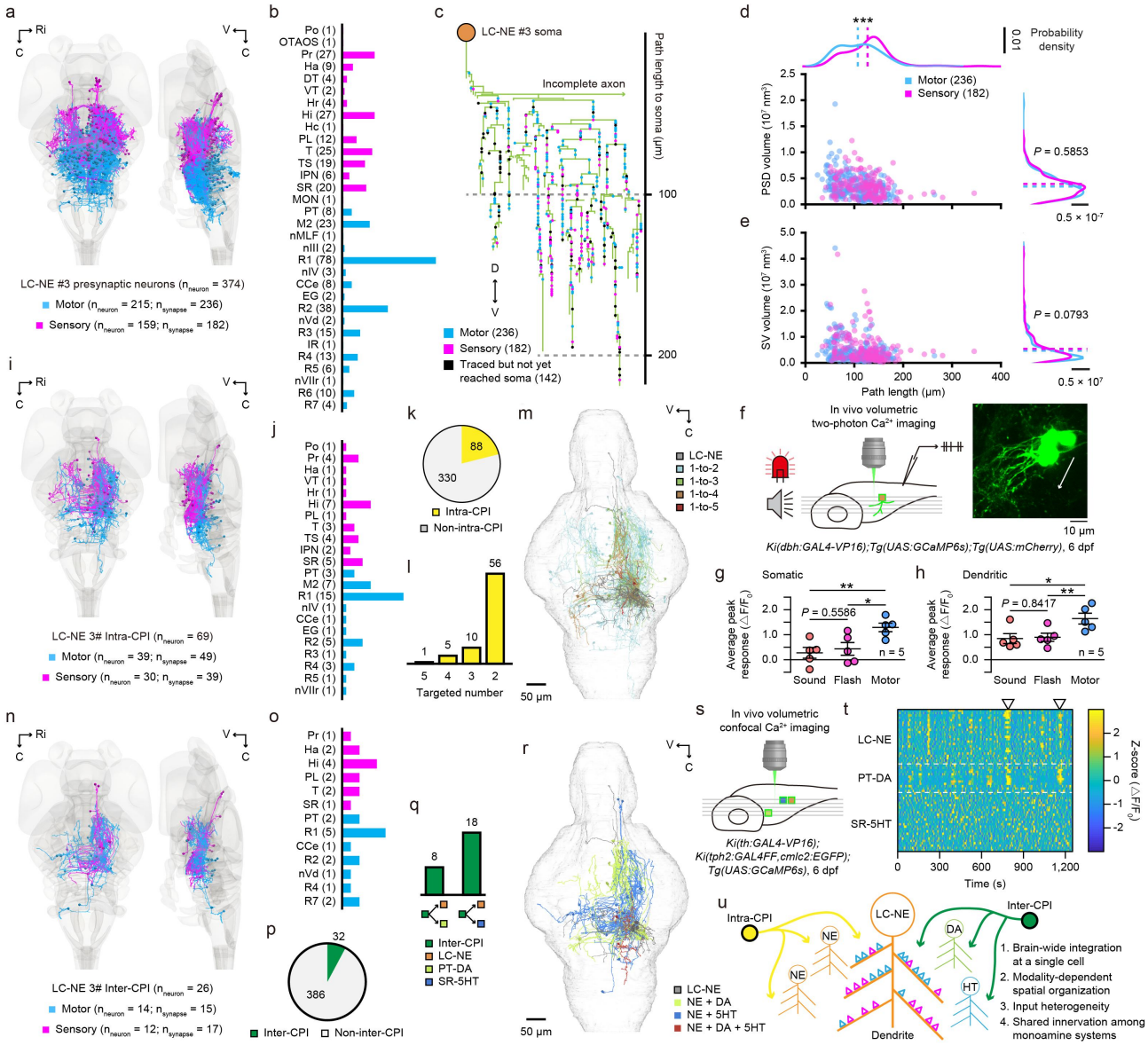
a
Ri
C
V
C
LC-NE #3 presynaptic neurons (n_neuron = 374)
Motor (n_neuron = 215; n_synapse = 236)
Sensory (n_neuron = 159; n_synapse = 182)
b
Po (1)
OTAOS (1)
Pr (27)
Ha (9)
DT (4)
VT (2)
Hr (4)
Hi (27)
Hc (1)
PL (12)
T (25)
TS (19)
IPN (6)
SR (20)
MON (1)
PT (8)
M2 (23)
nMLF (1)
nIII (2)
R1 (78)
nIV (3)
CCe (8)
EG (2)
R2 (38)
nVd (2)
R3 (15)
IR (1)
R4 (13)
R5 (6)
nVIIr (1)
R6 (10)
R7 (4)
c
LC-NE #3 soma
Incomplete axon
Path length to soma (μm)
100
200
D
V
Motor (236)
Sensory (182)
Traced but not yet reached soma (142)
d
***
0.01
Probability density
Motor (236)
Sensory (182)
PSD volume (10^7 nm^3)
P = 0.5853
0.5 × 10^-7
e
SV volume (10^7 nm^3)
P = 0.0793
0.5 × 10^7
Path length (μm)
i
LC-NE 3# Intra-CPI (n_neuron = 69)
Motor (n_neuron = 39; n_synapse = 49)
Sensory (n_neuron = 30; n_synapse = 39)
j
k
88
330
Intra-CPI
Non-intra-CPI
l
56
10
5
1
5 4 3 2
Targeted number
m
LC-NE
1-to-2
1-to-3
1-to-4
1-to-5
50 μm
f
In vivo volumetric two-photon Ca2+ imaging
Ki(dbh:GAL4-VP16);Tg(UAS:GCaMP6s);Tg(UAS:mCherry), 6 dpf
10 μm
g
Somatic
Average peak response (△F/F0)
P = 0.5586
n = 5
Sound Flash Motor
h
Dendritic
P = 0.8417
n = 5
Sound Flash Motor
n
LC-NE 3# Inter-CPI (n_neuron = 26)
Motor (n_neuron = 14; n_synapse = 15)
Sensory (n_neuron = 12; n_synapse = 17)
o
Pr (1)
Ha (2)
Hi (4)
PL (2)
T (2)
SR (1)
PT (2)
R1 (5)
CCe (1)
R2 (2)
nVd (1)
R4 (1)
R7 (2)
p
32
386
Inter-CPI
Non-inter-CPI
q
8
18
Inter-CPI
LC-NE
PT-DA
SR-5HT
r
LC-NE
NE + DA
NE + 5HT
NE + DA + 5HT
50 μm
s
In vivo volumetric confocal Ca2+ imaging
Ki(th:GAL4-VP16); Ki(tph2:GAL4FF,cmlc2:EGFP); Tg(UAS:GCaMP6s), 6 dpf
t
LC-NE
PT-DA
SR-5HT
Z-score (△F/F0)
Time (s)
u
Intra-CPI
LC-NE
Inter-CPI
NE
DA
HT
Dendrite
1. Brain-wide integration at a single cell
2. Modality-dependent spatial organization
3. Input heterogeneity
4. Shared innervation among monoamine systems

1551 **Extended Data Fig. 1**

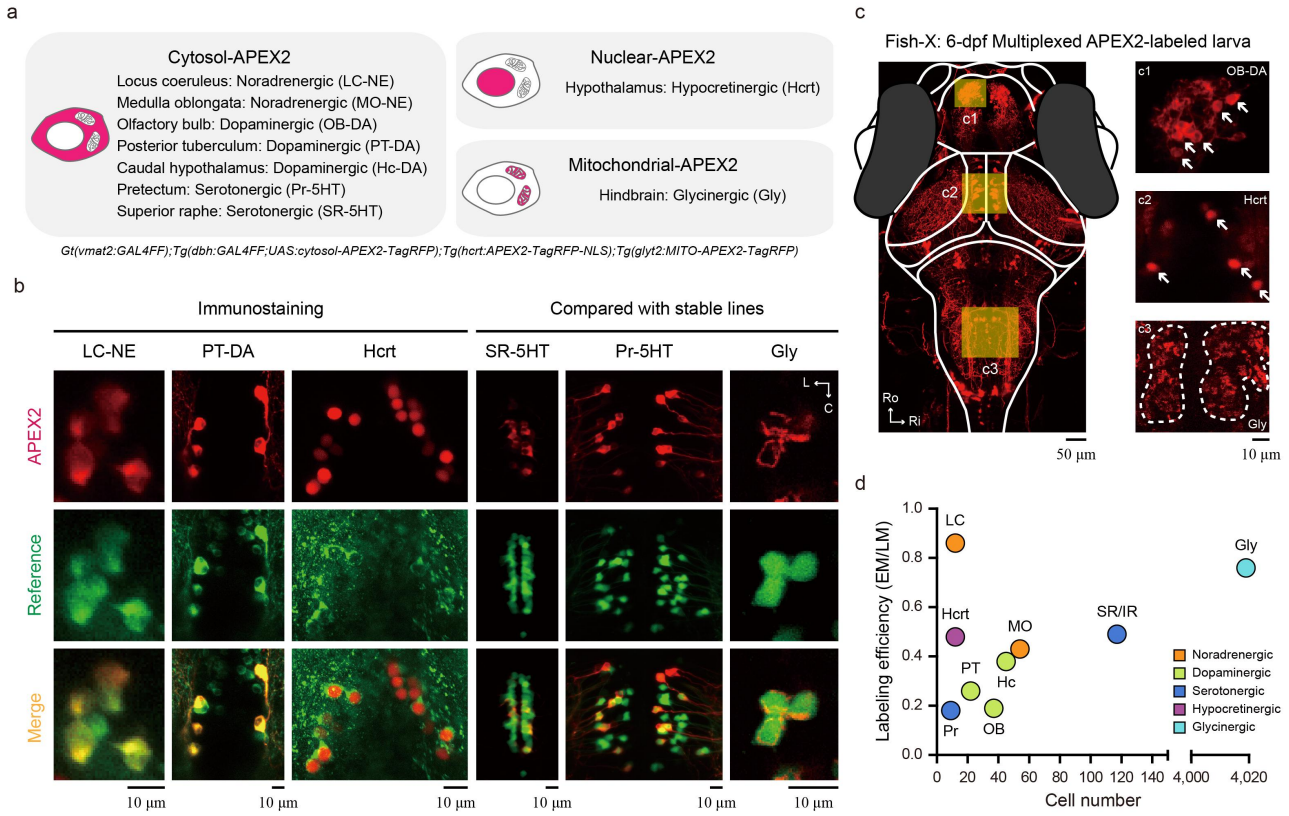

1552

1553

1554 **Extended Data Fig. 2**

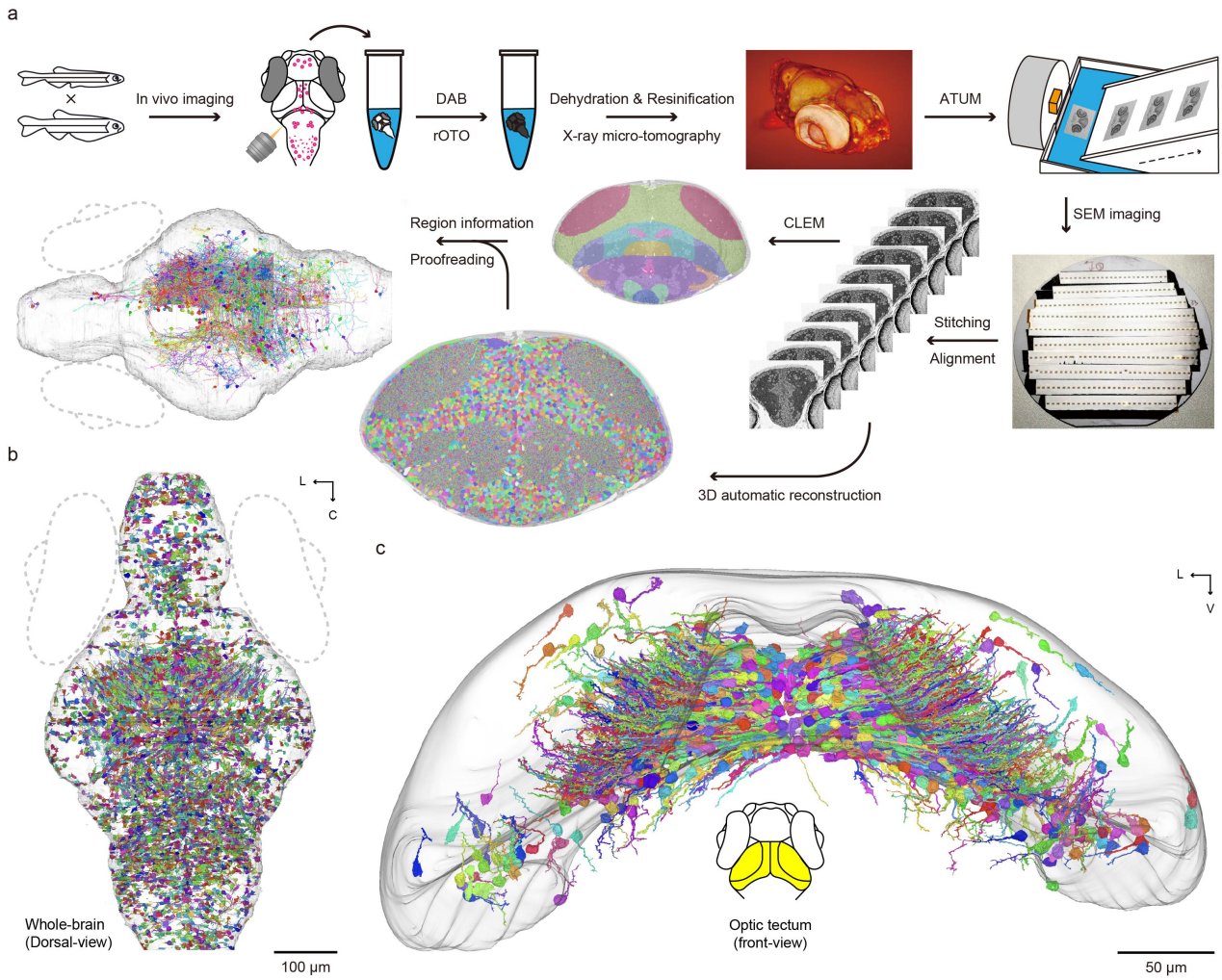

1555

1556

Extended Data Fig. 3

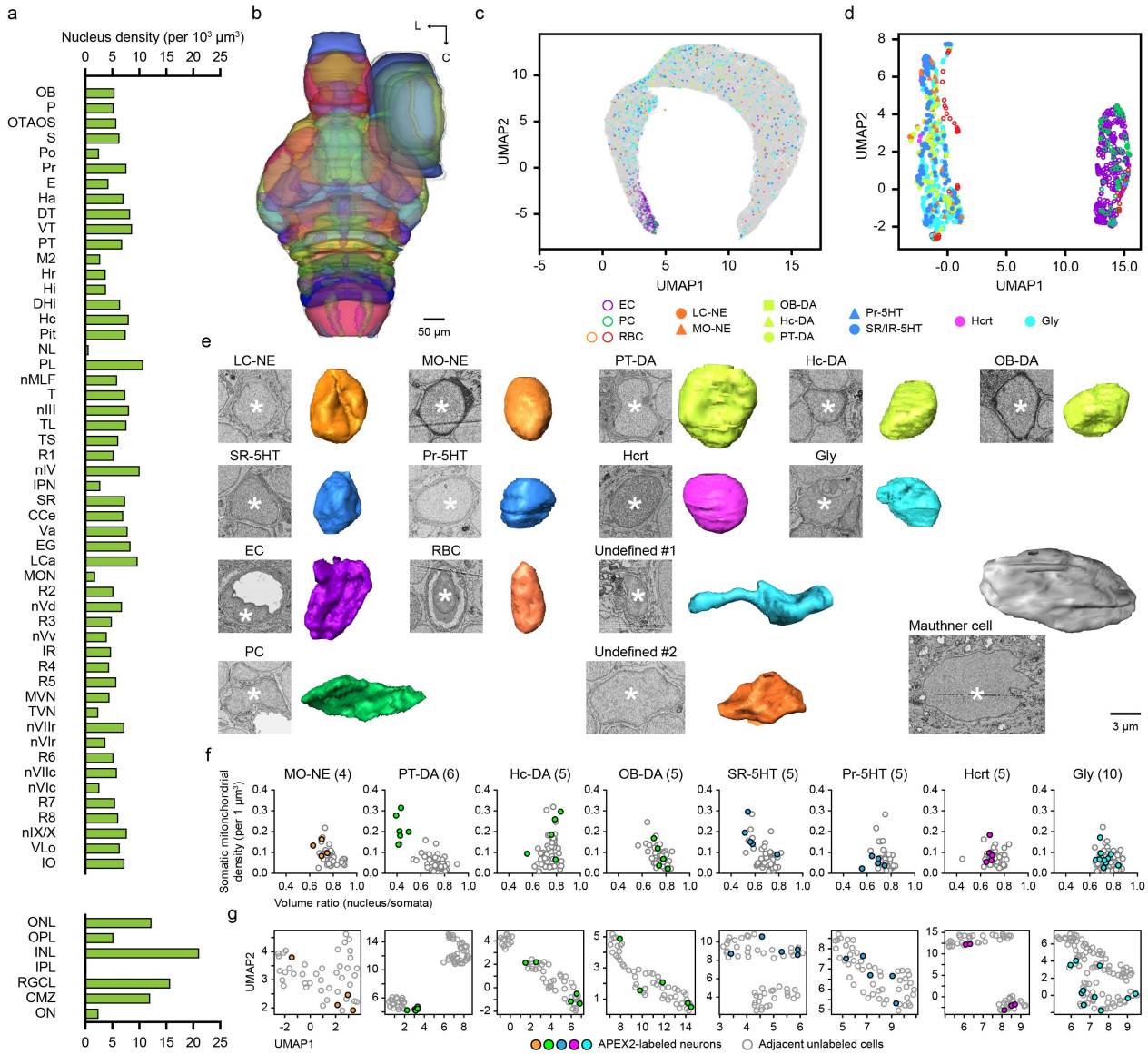

1560 **Extended Data Fig. 4**

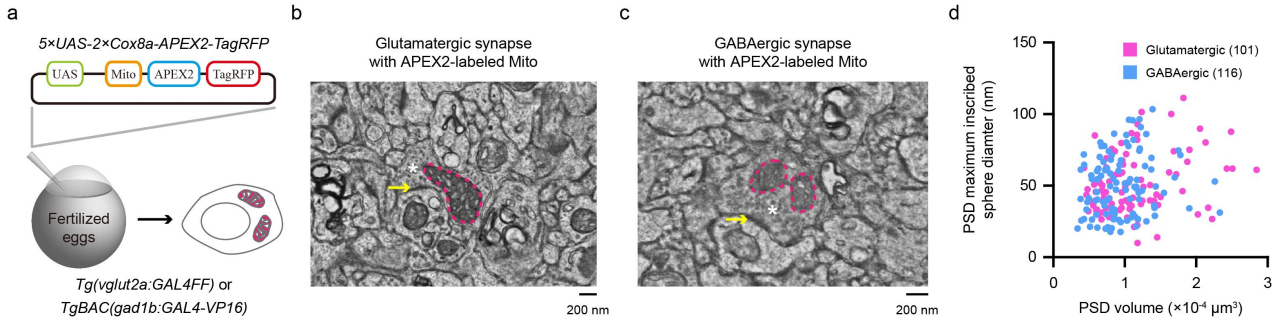

1561

1562

Extended Data Fig. 5

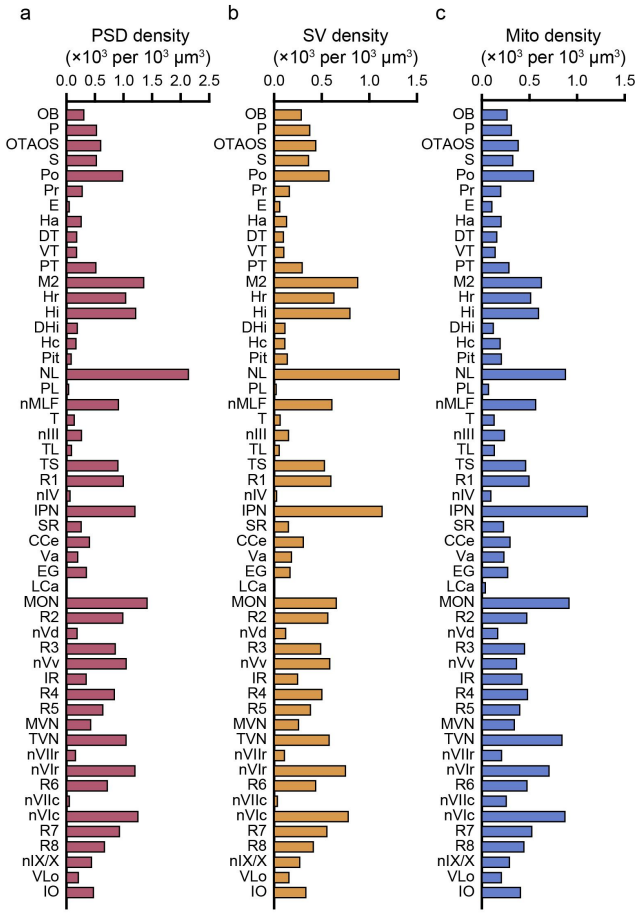

Extended Data Fig. 6

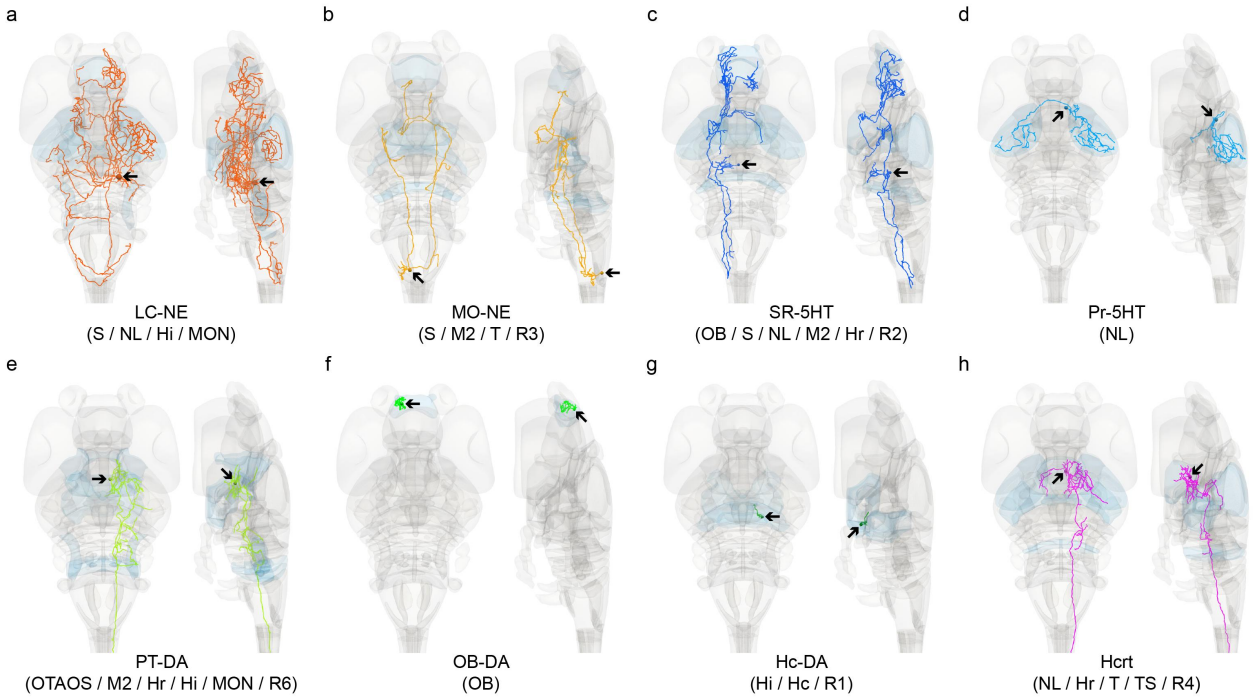

Extended Data Fig. 7

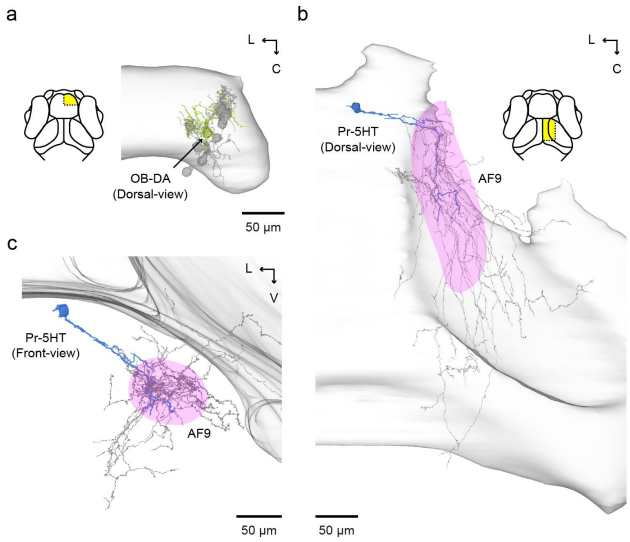

1572 **Extended Data Fig. 8**

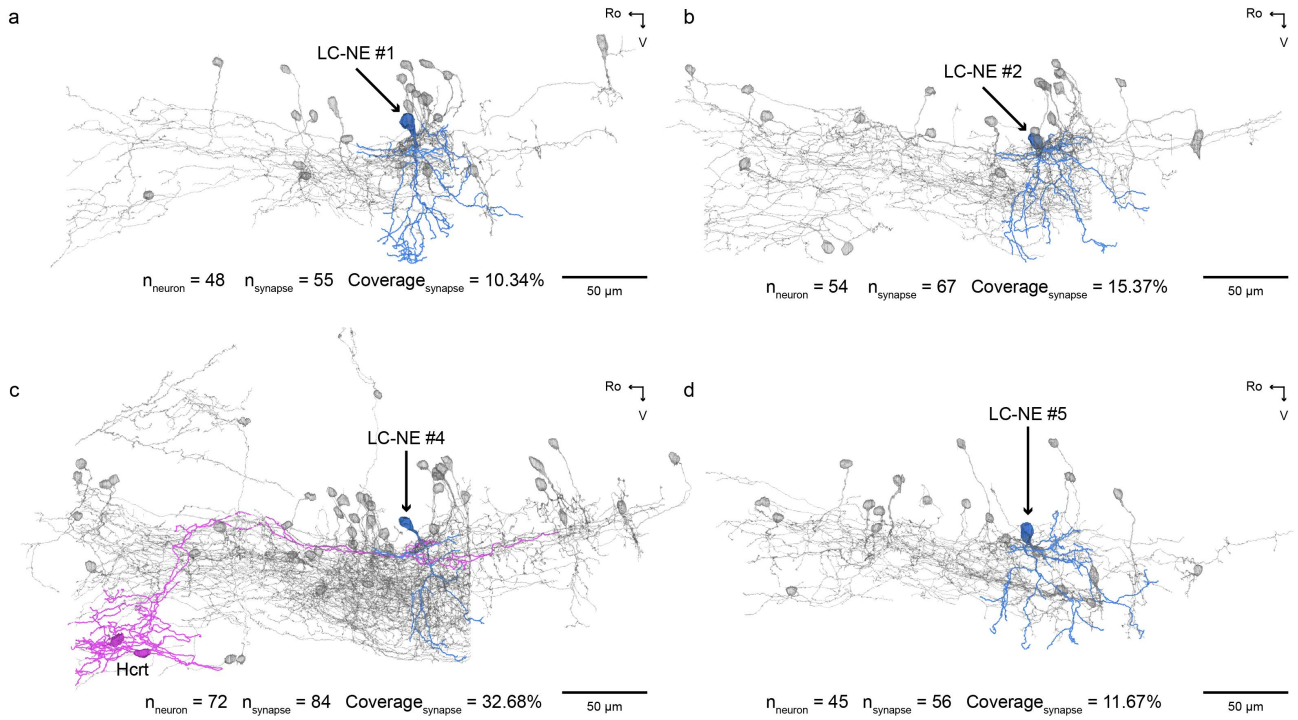

1573